Investigating the differences in calculating global mean surface CO_2 abundance: the impact of analysis methodologies and site selection

Zhendong Wu[1,2,*], Alex Vermeulen[2,*], Yousuke Sawa[3], Ute Karstens[1,2], Wouter Peters[4,5], Remco de ~~Kok[4]~~Kok[6], Xin ~~Lan[6]~~Lan[7,~~7~~8], Yasuyuki Nagai[3], Akinori Ogi[3], Oksana ~~Tarasova[8]~~Tarasova[9]

[1]ICOS Carbon Portal at Lund University~~, Department of Physical Geography and Ecosystem Sciences~~, Lund, Sweden
[2]ICOS ERIC, Carbon Portal, Lund, Sweden
[3]Japan Meteorological Agency (JMA), Tokyo, Japan
[4]Wageningen University, Wageningen, The Netherlands
[5]University of Groningen, Groningen, The Netherlands
[6]ICOS Carbon Portal at Wageningen University, Wageningen, The Netherlands
~~[6]NOAA~~ [7]NOAA Global Monitoring Laboratory (GML), Boulder, USA
~~[7]Cooperative~~ [8]Cooperative Institute for Research in Environmental Sciences, University of Colorado Boulder, USA
~~[8]WMO~~[9]WMO, Geneva, Switzerland

Correspondence to: Alex Vermeulen (alex.vermeulen@icos-ri.eu), and Zhendong Wu (zhendong.wu@nateko.lu.se)

Abstract. The World Meteorological Organization (WMO) Global Atmosphere Watch (GAW) coordinates high-quality atmospheric greenhouse gas observations globally and provides these observations through the WMO World Data Centre for Greenhouse Gases (WDCGG) supported by Japan Meteorological Agency. The WDCGG and the National Oceanic and Atmospheric Administration (NOAA) analyse these measurements using different methodologies and site selection to calculate global annual mean surface CO_2 and its growth rate as a headline climate indicator. This study ~~proposes~~ introduces a third hybrid method named ~~semi-NOAA~~GFIT, which serves~~is used~~ as an independent validation and open-source alternative ~~of~~ to the methods ~~as~~ described by NOAA and WDCGG. We apply ~~the semi-NOAA~~GFIT to incorporate observations from most WMO GAW stations and 3D modelled CO_2 fields from CarbonTracker Europe (CTE). We ~~found~~ find that different observational networks (i.e., ~~the~~ NOAA, GAW, and CTE networks) and analysis methods result in differences in the calculated global surface CO_2 mole fractions equivalent to the current atmospheric growth rate over a three-month period. However, the CO_2 growth rate derived from these networks and CTE model output shows good agreement. Over the long-term period (40 years), both networks with and without continental sites exhibit the same trend in the growth rate (0.030 ± 0.002 ppm per year each year). However, a clear difference emerges in the short-term (~~one~~ one-month) change ~~of~~ in the growth rate. The network that includes continental sites improves the early detection of changes in biogenic emissions.

1 Introduction

Global mean surface temperature averaged over 2011-2020 has increased by about 1.09°C relative to the average temperature of 1850–1900 (Gulev et al., 2021). The increasing amount of atmospheric carbon dioxide (CO_2), together with increases in other greenhouse gases, is the main driver of the warming (Eyring et al., 2021). After being relatively stable between 180 ppm

Formatted: Left: 1.65 cm, Right: 1.65 cm, Top: 1 cm, Bottom: 2.36 cm

Formatted: Superscript

Formatted: Affiliation

(ice age) and 280 ppm (interglacial) for the last 800,000 years (Lüthi et al., 2008), the annual average CO_2 level of the atmosphere has increased since the industrial revolution from roughly 277 ppm in 1750 to 415.7±0.2 ppm in 2021 (WMO, 2022), due to emissions of CO_2 related to human activities like burning of fossil fuels and land use changes (Friedlingstein et al., 2022). Mean global atmospheric CO_2 annual growth rate (G_{ATM}) is an important constraint on the global carbon cycle. Based on the most recent Global Carbon Budget (GCB) analysis (Friedlingstein et al., 2022), the total emission of CO_2 due to human activities was 10.2 ± 0.8 GtC yr^{-1} in 2020, of which 3.0 ± 0.4 GtC yr^{-1} was captured by the ocean sink and 2.9 ± 1 GtC yr^{-1} by the terrestrial sink, leaving a net increase of 5.0 ± 0.2 GtC yr^{-1} of CO_2 in the atmosphere, corresponding to an atmospheric CO_2 mole fraction increase of 2.4 ± 0.1 ppm yr^{-1} (the conversion factor comes from Ballantyne et al. (2012)).

As the atmosphere mixes the contributions of all sources and sinks, an observational global average CO_2 mole fraction can be constructed if there are enough observations to represent the spatial and temporal variation across the globe. Since most land masses are concentrated in the Northern Hemisphere, and the highest anthropogenic emissions (e.g. during winter) occur in the relatively narrow latitudinal band between 30 ºN and 60 ºN, relatively large spatial and temporal gradients in CO_2 mole fraction exist in and around that region. Due to convective and advective mixing, the average mixing time of air within the same latitudinal bands varies from several weeks to a month. However, mixing between latitudinal bands is slower, especially the exchange between the northern and southern hemispheres, which has an approximate interhemispheric transport time of 1.4 ± 0.2 years (Patra et al., 2011). The interplay of the latitudinal and interhemispheric differences in fossil fuel emissions and seasonal exchange with land biota (Denning et al., 1995) creates a latitudinal and interhemispheric gradient that requires a sufficiently dense network to capture a representative global annual mean.

However, measurement stations that are close to sources or sinks may not be representative of a large atmospherice volume and the average signal at their latitude. Therefore, inclusion of these observations might introduce ~~significant~~ biases on the global mean CO_2 and its growth rate. These biases can be avoided by filtering of data and a careful selection of spatially representative stations, as done by NOAA in their use of 43 stations (Fig. 1) that are considered to be representative for the Marine Boundary Layer (MBL reference network, https://www.esrl.noaa.gov/gmd/ccgg/mbl/mbl.html). An additional data processing step developed by NOAA to further avoid biases due to unrepresentative local signals is filtering and smoothing, by using a combination of a low pass filter and decomposition into a fitted long-term trend and seasonal cycle (Thoning et al., 1989), hereafter refered to as the NOAA analysis. These fits can also be used to fill gaps for missing data, though care must be taken to avoid extrapolation errors before and beyond the time covered by the data record of the station. The WMO Global Atmosphere Watch (GAW) World Data Centre for Greenhouse Gases (WDCGG) ~~also~~ publishes global averages mole fraction for CO_2 and the other major greenhouse gases in the annual WMO GAW Greenhouse Gas Bulletin (latest version: WMO, 2022). They use curve fitting and filter methods that are very similar to those developed by NOAA, but WDCGG includes continental locations that are potentially more influenced by local sources and sinks (Tsutsumi et al., 2009).

The NOAA MBL observations are all part of the NOAA cooperative global air sampling network and analysed in the same laboratory. All NOAA flask-air observations are traceable to the current WMO X2019 CO_2 scale that is maintained by NOAA Global Monitoring Laboratory (GML). In contrast, the WDCGG data originate from multiple independent laboratories (including NOAA GML), that together form a network of hundreds of stations coordinated by WMO GAW [http://gawsis.meteoswiss.ch]. Having a multitude of independent laboratories carries an additional risk of biases due to differences in sampling, measurement, and analysis methods, for example calibration scales, although much care is taken to avoid these by coordination in the network and use of a common calibration scale from ~~the~~ WMO Central Calibration Laboratories~~y~~ (CCL) guided by a set of strict measurement compatibility goals (WMO, 2022). The different selection of stations results in a larger seasonal cycle amplitude in WDCGG results compared to those of NOAA and a small but quite consistent bias in global surface annual mean CO_2 mole fraction (Tsutsumi et al., 2009). The NOAA estimate of global surface annual mean CO_2 mole fraction is expected to be ~~negatively biased~~lower (e.g. ~0.35 ppm lower than the WDCGG estimate,

Formatted: Hyperlink

Tsutsumi et al., 2009) compared to a full global surface average because areas with large sources are not represented. However, ~~none of~~ the two afore~~-~~mentioned approaches neither represent~~s~~ the~~ose~~ parts of~~that have~~ the atmosphere with low CO_2 mole fraction levels~~,~~ (i.e., the full troposphere, ~~(~~up to ~8-15 km altitude~~,)~~ and the stratosphere), nor do they cover~~, or~~ the regions of the world with substantial observational gaps.

In this paper, we propose a data integration method to estimate the global mean surface CO_2 and its growth rate, named ~~semi-NOAA~~GFIT~~,~~. This method serves as~~which is used as~~ an independent validation of the methods as described by NOAA and WDCGG through a completely independent and open-source implementation. The global mean surface CO_2 refers to the mean CO_2 mole fraction within the planetary boundary layer, which extends from the Earth's surface up to a few hundred or thousand meters in height. We apply the ~~semi-NOAA~~GFIT methodology to incorporate CO_2 data from the GAW network (139 stations, Fig. 1) and the modelled CO_2 distribution from a well-established 3D global transport model (TM5: Transport Model 5, Peters et al., 2004, Krol et al., 2005). We investigate the influence of small differences between the three methodologies and whether these are significant or not for calculating the global mean surface CO_2 and its growth rate, how consistent the ~~semi-NOAA~~GFIT and WDCGG approaches are with each other, and how they compare with NOAA analysis and estimates derived from a CO_2 simulation with the 3D transport model TM5. These 3D CO_2 results for 2001-2020 using TM5 are performed in the CarbonTracker Europe framework (CTE, Peters et al., 2004, van der Laan-Luijkx et al., 2017), where the CO_2 uptake and emission fluxes are optimized by the inversion system to minimize the mismatch between the *in situ* observations and the modelled CO_2 mole fraction. CTE generally has a good representation of the CO_2 field, with mean biases with respect to independent aircraft measurements of generally less than 0.5 ppm (Friedlingstein et al., 2022). Furthermore, the inferred CO_2 fluxes from CTE fit well within the ensemble of those of other inversions used for the evaluation of Global Carbon Budget (e.g. Friedlingstein et al., 2022).

2 Methods and data

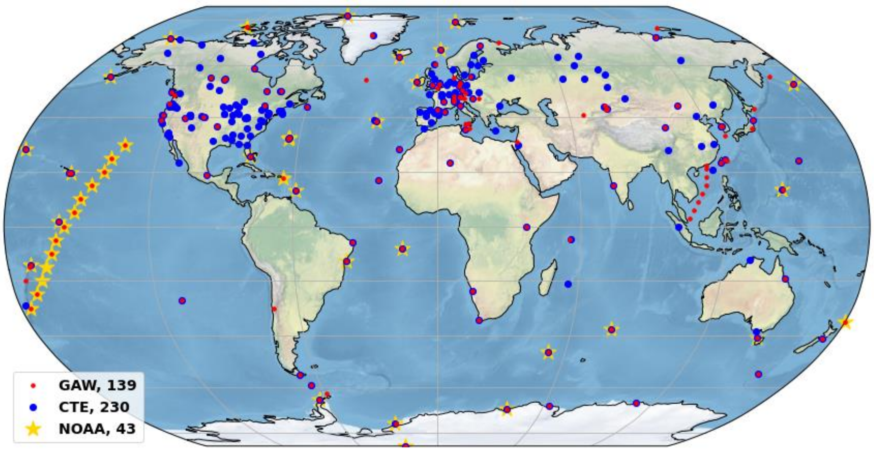

Figure 1. **Three observation networks are employed to assess the impact of continental site inclusion when calculating global CO_2 mole fraction and its growth rates. The NOAA network (43 sites, yellow stars) comprises MBL sites only. The selected GAW global network ~~for CO_2 measurement~~ (139 sites, red dots) includes both MBL sites and continental sites, for example from the Advanced Global Atmospheric Gases Experiment (AGAGE) and European ICOS contribution network. The~~,~~ CTE network serves as the global network for the CTE model evaluations (230 sites, blue dots), comprises MBL sites and a more extensive inclusion of continental sites~~and the NOAA network (43 sites, yellow stars)~~.**

Formatted: Subscript

Formatted: Subscript

Formatted: Subscript

2.1 The WMO GAW observations and WDCGG analysis method

The WMO GAW network measurements are archived and distributed by WDCGG~~, (World Data Center for Greenhouse Gases),~~ hosted by the Japan Meteorological Agency. The GAW observations used in this study originate from 139 selected stations of the GAW network, and all observations are on the WMO standard scale, WMO-CO_2-X2019 (Hall et al., 2021). The details on the station selection are described in Tsutsumi et al., (2009), which mainly excludes stations located in the northern hemisphere that show large standard deviations from the latitudinal fitted curve. The remaining 139 stations show a more reasonable latitudinal scatter range (Fig. 1).

The WDCGG global analysis method (hereafter WDCGG method), as described in Tsutsumi et al., (2009), includes the mentioned station selection, a data fitting and filter (involves data interpolation and extrapolation), and calculation of the zonal and global mean mole fractions, trends, and growth rates. The procedure is also summarized in Text S1.

The output from the global analysis by the WDCGG method ~~are~~ is used to compare against an alternative method (~~semi-NOAA~~GFIT) that we designed to follow as closely as possible the fit and filter method (Conway et al., 1994) deployed by NOAA and is described in the section 2.3.

2.2 CTE model output and station observations

CarbonTracker Europe (CTE) is a global model of atmospheric CO_2 and designed to keep track of CO_2 uptake and release at the Earth's surface over time (van der Laan-Luijkx et al., 2017). CTE incorporates an off-line atmospheric transport module (TM5, Peters et al., 2004, Krol et al., 2005) driven by ECMWF ERA5 data, and there are four prescribed fluxes (i.e. from ocean, biosphere, fire and fossil fuel), which are transported in the model, together with the transported initial CO_2 field. CTE also includes a data assimilation system that applies an ensemble Kalman filter to optimize the biogenic and ocean fluxes for a combination of plant-functional types and climate zones to improve the fit of the simulated concentrations with observations. The optimized fluxes from the data assimilation have been used in Global Carbon Project (GCP) 2021 ~~(Friedlingstein et al., 2022)~~, and the comparison of CTE CO_2 product to the other data assimilation systems used in GCP shows good agreement (within 0.8 ppm at all latitude bands)~~and CTE compares well to the other data assimilation systems used in GCP~~ (Friedlingstein et al., 2022).

The CTE model data used here ~~consisted~~ consists of simulated monthly CO_2 mole fraction at 1x1 degree horizontal resolution and 25 levels in the vertical, the data period ranges from 2001 to 2020 which has no influence of model spin-up (Krol et al., 2018). From the CTE output a set of simulated synthetic atmospheric CO_2 mole fractions with monthly resolution can be extracted within grid cells where stations are situated. This study analyses monthly observation data (1980-2020) and synthetic time series (2001-2020) by using the ~~semi-NOAA~~GFIT method (section 2.3) and attempts to estimate global mean CO_2 mole fraction and its growth rate. The observed CO_2 mole fractions are taken from 230 out of 290 global-wide distributed stations (Fig. 1, the station selection is summarized in Text S2), the data come from the GLOBALVIEW-plus V8 ObsPack data product (Schuldt et al., 2022)~~(Kenneth N., 2022)~~, and include surface-based, shipboard-based and tower-based measurements.

Formatted: Font color: Auto

Formatted: Font color: Auto

2.3 The ~~semi-NOAA~~GFIT method

The temporal pattern of CO_2 measurement records at locations around the globe can be explained as the combination of roughly three components: a long-term trend, a non-sinusoidal yearly cycle (or seasonality), and short-term variations. This study synchronizes monthly CO_2 records with the fitting and filter method ~~obtained~~ developed at~~from~~ the NOAA Global Monitoring Laboratory (Thoning et al., 1989, Conway et al., 1994), without extrapolation. The station selection and CO_2 averaging method are kept the same as in the WDCGG method (Text S1). This method will be referred to as the ~~semi-NOAA~~GFIT method and will be compared to the WDCGG method without extrapolation. The only difference from WDCGG method without extrapolation is the fitting and filter method. All code for the method described here was developed in Python and is available as a Jupyter notebook under a GPL license [https://doi.org/10.18160/Q788-9081]. The ~~semi-NOAA~~GFIT method can be summarized and illustrated by the following three steps.

2.3.1. Fitting and filter

CO_2 records from each station can be abstracted as a combination of long-term trend and seasonality, which can be fitted by a function consisting of polynomial and harmonics. We applied a linear regression analysis based on 3 polynomial coefficients and 4 harmonics (Eq. 1) to fit CO_2 data using general linear least-squares fit (LFIT, Press et al., 1988).

$$f(x) = a_0 + a_1 t + a_2 t^2 + \cdots + a_k t^k + \sum_{n=1}^{n_h} (A_n \cos 2\pi n t + B_n \sin 2\pi n t) \quad (1)$$

where a_k, A_n and B_n are fitted parameters, t is the time from the beginning of the observation and it is in months and expressed as a decimal of its year. k denotes polynomial number, $k = 2$. n_h denotes harmonic number, $n_h = 4$. Fig. 2 illustrates the function fit to CO_2 data to ~~gain~~ obtain the annual oscillation (red line in Fig. 2a), is a combination of a polynomial fit to the trend (blue line in Fig. 2a) and harmonic fit to the seasonality (green line in Fig. 2b).

The residuals are the difference between raw data and the function fit (black dots in Fig. 2c). The filtering method is based on Thoning et al. (1989) which transforms CO_2 data from time domain to frequency domain using a Fast Fourier Transform (FFT), then applies ~~of~~ a low pass filter to the frequency data to remove high-frequency variations, and then transforms the filtered data back to the time domain using an inverse FFT. The short term (a cut-off value of 80 days, red line in Fig. 2c) and long term (a cut-off value of 667 days, blue line in Fig. 2c) filters used here are the same as in NOAA method, and applied to obtain the short term and interannual variations that are not determined by the fit function. The original ~~part of the~~ code is also available as Python code from the NOAA website [https://gml.noaa.gov/aftp/user/thoning/ccgcrv/].

2.3.2. Calculate smoothed CO_2 and long-term trend

The result~~s~~ of ~~the~~ filtering residuals are ~~then~~ added to the fitted curve to obtain smoothed CO_2 and its long-term trend. The smoothed CO_2 comprises ~~the~~ fitted trend, ~~the~~ fitted seasonality and ~~the~~ smoothed residuals (red line in Fig. 2d), ~~which only~~the latter removes only short-term variations or noise. The long-term trend comprises fitted trend and residual trend, which removes seasonal cycle and noise (blue line in Fig. 2d).

2.3.3. Calculate CO_2 growth rate, G_{ATM}

The CO_2 growth rate (G_{ATM}) ~~G_{ATM}~~ is determined by taking the first derivative of the long-term trend. However, the growth is made up of discrete points, e.g. the black dots in Fig. 3a shows the trend points. In this case, a cubic spline interpolation is applied to the trend points, in which the spline curve passes through each trend points, as the blue line in Fig. 3a. G_{ATM} is obtained by taking the derivative of the spline at each trend point (Fig. 3b).

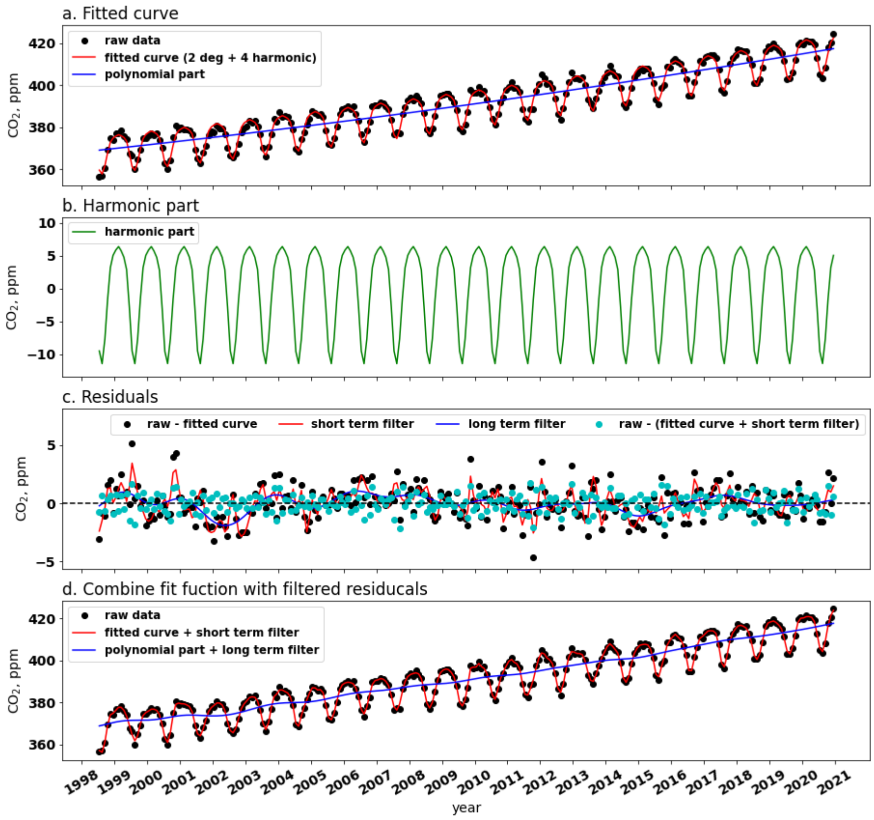

Figure 2. Example of analysed CO_2 data from ~~PAL~~ station ~~(~~Pallas (PAL, Finland), illustrating ~~semi-NOAA~~GFIT curve fitting and filter method. Panel (a) shows monthly averaged CO_2 (dots), curve fitting with 2-degree polynomial and 4-degree harmonics (red line), and long-term trend estimated by a 2-degree polynomial (blue line). Panel (b) shows seasonality estimated by 4-degree harmonics. Panel (c) shows the residuals of raw data from the function fit (black dots), the red line is obtained by the short-term filter and the blue line is obtained by the long-term filter. The cyan dots show the residuals of raw data from the sum of fitted curve and smoothed residuals. Panel (d) shows final processed CO_2, which comprises fitted trend, fitted seasonality and smoothed residuals (red line). The blue line shows the final trend which comprises fitted trend and residuals trend.

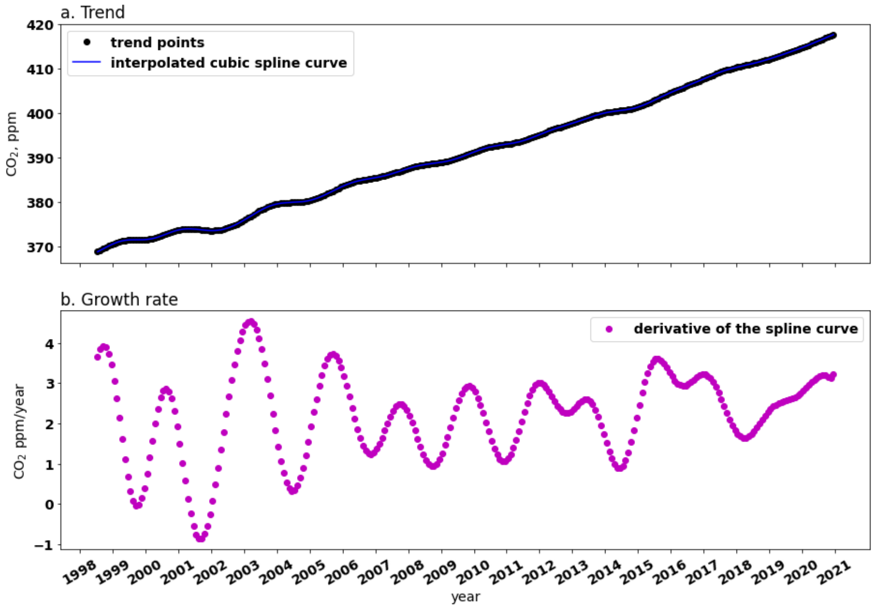

Figure 3. Example of CO_2 growth rate, the raw data is the same as used in Fig. 2 from station ~~PAL (~~Pallas (PAL, Finland). Panel (a) shows the trend points (black dots) and its cubic spline interpolation (blue line). Panel (b) shows the G_{ATM} at each trend point.

3 Results

Global averaged surface CO_2 and its G_{ATM} are calculated ~~from the GAW observations from 139 sites (Fig. 1)~~ using the WDCGG method ~~with and without extrapolation~~ and our ~~semi-NOAA~~GFIT method based on the data from the GAW and CTE networks (Fig. 1). ~~, namely GAW (WDCGG+), GAW (WDCGG) and GAW (semi-NOAA)~~The different observation networks and their analysis methods are listed in Table 1. ~~The semi-NOAA method is also applied to three CTE datasets: 1) observations from 230 sites selected in the CTE dataset (hereafter these sites are named as CTE network, Fig. 1) which comes from the ObsPack data product (Kenneth N., 2022), namely CTE_obs (semi-NOAA); 2) CTE model output at the sites (sampled at the same location, altitude and time), namely CTE_output (semi-NOAA); and 3) model output for full global grids (averaged over the first three levels, 0 to 0.35 km Alt.), namely CTE_global (semi-NOAA).~~ We calculated the global means and its G_{ATM} by area-weighted averaging the zonal means over each latitudinal band (30°), ~~as same as~~following the same CO_2 averaging ~~method~~method as described in Tsutsumi et al. (2009). A bootstrap method is used to estimate the uncertainties of global CO_2 mean and its G_{ATM}, which is an almost identical uncertainty analysis as presented by Conway et al. (1994) who constructed 100 bootstrap networks for the NOAA analysis. We construct 200 bootstrap networks, ~~which is~~ consistent with the WDCGG analysis in Tsutsumi et al., (2009). For each bootstrap network, we randomly draw the same number of sites ~~(~~as the actual network~~,~~ (e.g. 139 sites for GAW network) with replacement ~~(or restitution)~~ from the actual network, which means some sites are missing whereas others will be represented twice or more often. We calculate global mean CO_2 mole fraction and its G_{ATM} for each network, and then calculate the statistics (i.e. mean and 68% confidence interval, CI) on the 200 networks. All uncertainties in this paper are reported as ± 68% CI.

Table 1. Description of the three observation networks and their analysis methods.

Formatted: Font color: Auto

Terminology	Description
NOAA network	NOAA network comprises MBL sites only (43 sites).
GAW network	The selected GAW global network (139 sites) includes both MBL sites and some continental sites.
CTE network	The CTE network serves as the global network for the CTE model evaluations (230 sites), comprises MBL sites and a more extensive inclusion of continental sites.
GAW (GFIT)	GAW network observations analysed using the GFIT method
GAW (WDCGG)	GAW network observations analysed using the WDCGG method without extrapolation
GAW (WDCGG+)	GAW network observations analysed using the WDCGG method with extrapolation
CTE_obs (GFIT)	CTE network observations analysed using the GFIT method. The observations come from the ObsPack data product (Schuldt et al., 2022)
CTE_output (GFIT)	CTE model output at the 230 sites (sampled at the same location, altitude and time) analyzed using the GFIT method
CTE_global (GFIT)	CTE model output for full global grids (averaged over the first three levels, 0 to 0.35 km Alt.) analysed using the GFIT method
MLO (GFIT)	Mauna Loa (MLO) observations analysed using the GFIT method
SPO (GFIT)	South Pole (SPO) observations analysed using the GFIT method

3.1 Globally averaged surface CO_2 mole fraction and its G_{ATM}

Formatted: Normal

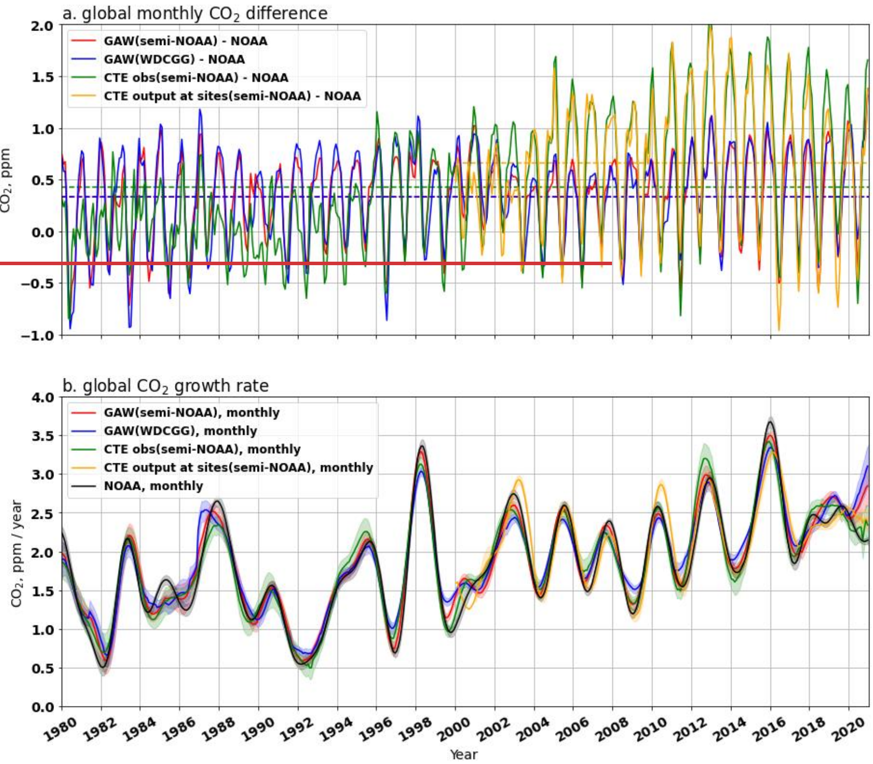

215

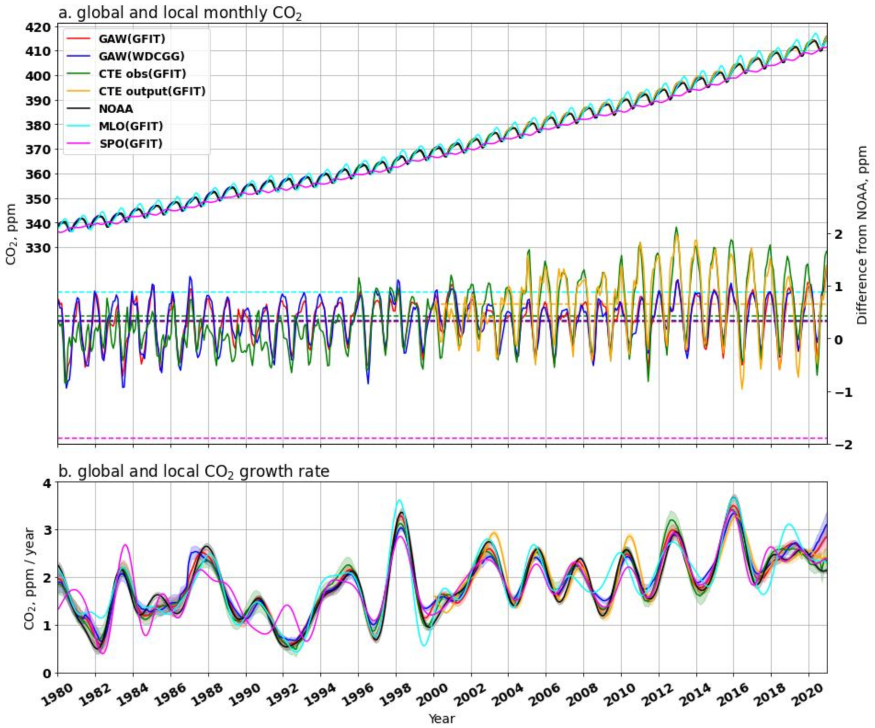

Figure 4. Comparison of globally and locally averaged CO_2 mole fraction (a) and its G_{ATM} (b) from 1980 to 2020. Panel (a) shows the global monthly CO_2 mole fraction from 139 GAW sites (estimated from observations only), 43 NOAA MBL sites and those from 230 sites used in CTE (either from observations or model output). The two local CO_2 mole fractions are from Mauna Loa (MLO, cyan line) and South Pole (SPO, magenta line) stations, analysed using the GFIT method. The red and blue lines show the CO_2 derived from GAW (GFIT) and GAW (WDCGG), respectively. The green and orange lines show the CO_2 derived from CTE_obs (GFIT) and CTE_output (GFIT), respectively. The right y-axis shows their difference from NOAA CO_2 mole fraction, and the dashed lines show the mean of the difference over the available period. Panel (b) compares the corresponding global and local CO_2 growth rate, the legend refers to panel (a). The shadow area shows the uncertainty as 68% confidence interval obtained by the bootstrap analysis.~~Comparison of globally averaged CO_2 mole fraction (a) and its G_{ATM} (b) from 1980 to 2020. Panel (a) shows the global monthly CO_2 mole fraction from 139 GAW sites (estimated from observations only) and those from 230 sites used in CTE (either from observations or model output) differs from NOAA estimates based on 43 MBL sites. Red and blue lines show the CO_2 derived from the GAW observations using semi-NOAA and WDCGG method without extrapolation, respectively. Green and orange lines show the CO_2 derived from observations and model output at the 230 sites assimilated by CTE using semi-NOAA method, respectively. The dash lines show the mean over the available period. Panel (b) compares the global CO_2 growth rate derived from GAW observations using semi-NOAA (red line) and WDCGG method without extrapolation (blue line), CTE observations (green line) and model output (orange line) using semi-NOAA method, and the NOAA analysis (black line). The shadow area shows the uncertainty as 68% confidence interval obtained by the bootstrap analysis.~~

Fig. 4 presents a monthly comparison of globally and locally averaged CO_2 mole fractions and their G_{ATM} from 1980 to 2020. The statistical metrics assessing the agreement of these monthly comparisons are available in Fig. 5 (for 2001-2020) and Fig. S1 (for 1980-2020). The statistical metrics for the annual comparisons can be found in Fig. S2 (for 2001-2020) and Fig. S3 (for 1980-2020). They exhibit a similar pattern to the monthly comparisons (i.e. Fig.5 and Fig. S1).

G~~G~~lobally ~~-~~averaged monthly surface CO_2 mole fractions, derived from the GAW network (GAW (~~semi-NOAA~~GFIT) or GAW (WDCGG)), are~~is~~ significantly ($p<0.05$) higher by 0.~~329~~ ~~329 or~~ 0.335~~36~~ ppm during 1980-2020 (Fig. S1a) and 0.370-0.390 ppm during 2001-2020 (Fig. 5a) ~~significantly (p<0.05) higher than~~when compared to the NOAA analysis ~~during 1980-~~

Formatted: Font: 10 pt

Formatted: Font: 10 pt

Formatted: Font: 10 pt

Formatted: Font: 10 pt

Formatted: Font: 10 pt

Formatted: Font: 10 pt

Formatted: Font: 10 pt

Formatted: Font: 10 pt

Formatted: Font: 10 pt, Subscript

Formatted: Font: 10 pt

~~2020~~ (~~red or blue line in Fig. 4a, Table S1a-b~~Fig. 4a)~~,). T~~this ~~result~~ finding aligns~~is consistent~~ with Tsutsumi et al., (2009), who reported~~found~~ a 0.350~~0~~ ppm higher global average in the GAW network during 1983-2006. The higher estimate from the GAW network can be ~~explained by~~attributed to the inclusion of more diverse sites, encompassing not only NOAA's MBL sites~~,~~ but also ~~more~~ additional continental sites (Fig. 1).

Both global CO_2 and its G_{ATM} derived from the GAW (~~semi-NOAA~~GFIT) and GAW (WDCGG) are nearly overlapping (the red and blue lines) in Fig. 4a~~a~~ and 4b~~b (as can also be seen by comparing Fig. S1 and S2)~~. The statistical metrics (~~Table S1a~~Fig. 5 and S1) ~~show~~ indicate a high agreement (ME<0.020 ppm, ~~r=0.999,~~ RMSE<~~=~~0.~~053~~ 145 ppm, r>0.999 ~~ME=0.007 ppm~~ for ~~the~~ CO_2 mole fraction; ME<0.005 ppm, ~~r=0.991,~~ RMSE<~~=~~0.108~~081~~ ppm yr^{-1}, ~~ME=0.005~~r>0.982 ~~ppm yr^{-1}~~ for ~~the~~ G_{ATM}) between these two methods, which confirms that the ~~semi-NOAA~~GFIT method agrees well with WDCGG method without extrapolation. The WDCGG method with extrapolation (i.e. GAW (WDCGG+)), ~~where~~ which involves extrapolating the long-term trend of each station ~~is extrapolated~~ to match the period of the most long-running station ~~period~~ and adding ~~ited~~ to the~~its~~ average seasonal variation to synchronize data period of all stations (Tsutsumi et al., 2009), produces ~~~~~0.096 ppm significantly ($p<0.05$) higher values than the global monthly surface CO_2 mole fraction derived from the GAW (WDCGG) during the common period 1984-2020 (~~see~~ Table ~~S2~~S1~~),~~). However, ~~while~~ the extrapolation has a minimal~~tiny~~ effect (RMSE=0.~~062~~ 076 ppm yr^{-1}, ME=-0.011 ppm yr^{-1}, Table ~~S2~~S1) on the CO_2 growth rate.

~~Global~~ Globally averaged monthly surface CO_2 derived from CTE_obs (~~semi-NOAA~~GFIT) and CTE_output (~~semi-NOAA~~GFIT) are 0.~~422~~ 422 ppm (1980-2020, Fig. S1) ~~(1980-2020)~~ and 0.~~656~~ 668 ppm (2001-2020, Fig. 5) ~~(2001-2020)~~ significantly ($p<0.05$) higher compared to the NOAA analysis ~~analysis~~, respectively (~~green and orange lines in~~ Fig. 4a~~a~~). Comparing the global mean of CTE_obs (~~semi-NOAA~~GFIT) with CTE_output (~~semi-NOAA~~GFIT) during the common period of 2001-2020, we ~~find~~ observe a low bias (0.069 ppm in CTE_output, ~~Table S1d-e and Table S~~Fig 5a~~3~~), which suggests~~indicates~~ that the CTE model results can reasonably reproduce the global mean CO_2 levels ~~reasonably well~~. The global annual CO_2 mole fraction from CTE_obs (~~semi-NOAA~~GFIT), CTE_output (~~semi-NOAA~~GFIT) and CTE_global (~~semi-NOAA~~GFIT) is 0.~~368~~367 ~~(2001-2020)~~, 0.299 ~~(2001-2020)~~ and 0.186 ~~(2001-2020)~~ ppm significantly ($p<0.05$) higher than the result of the GAW (~~semi-NOAA~~GFIT), respectively (Fig 5a~~Table S1d-f~~). The higher global mean from CTE_obs (~~semi-NOAA~~GFIT) and CTE_output (~~semi-NOAA~~GFIT) ~~is mainly due~~can be attributed to the presence of more sites in the Northern Hemisphere within the CTE network compared to the GAW network. The lower bias observed between GAW (~~semi-NOAA~~GFIT) and CTE_global (~~semi-NOAA~~GFIT) ~~indicates~~ suggests that the GAW network provides a good representation of the low-level atmosphere (i.e. 0 to 0.35 km altitude) at global scale ~~(Table S1f)~~, or the CTE model ~~has a good~~ performs well~~ance~~ in the low-level atmosphere.

A common approach to estimate global surface CO_2 mole fraction is by using one or two representative sites, such as Mauna Loa (MLO) and South Pole (SPO). The globally averaged monthly surface CO_2 mole fractions, derived from the GAW, CTE, and NOAA networks, are significantly ($p<0.05$) lower by 0.46-0.88 ppm during 1980-2020 (Fig. S1a) and 0.45-1.19 during 2001-2020 (Fig. 5a) than the local CO_2 estimates solely based on MLO measurements. Conversely, these global monthly CO_2 mole fractions are significantly ($p<0.05$) higher by 1.91-2.24 ppm during 1980-2020 (Fig. S1a) and 2.21-2.94 during 2001-2020 (Fig. 5a) when compared to local measurements at SPO site. Furthermore, the global seasonal cycle leads the local cycle at MLO by approximately one month (estimated by averaging the time difference between the peaks of their seasonal cycles). In contrast, the local cycle at SPO is not evident and is opposite to the global seasonal cycle (Fig. 4a).

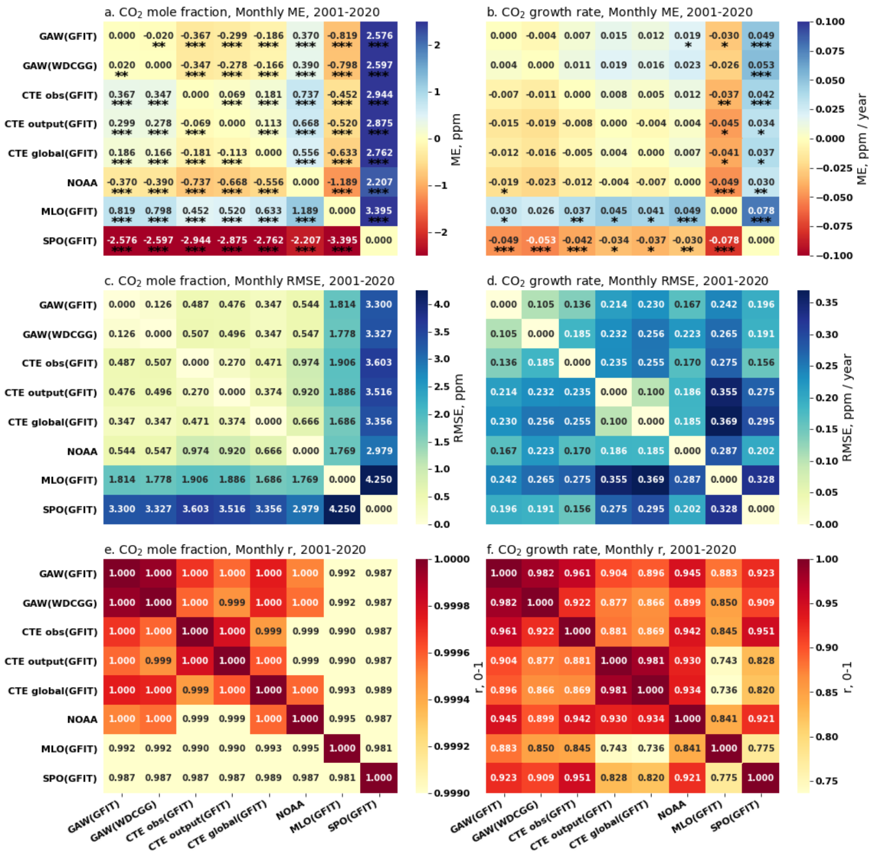

Figure 5. Pair-wise statistical metrics assess the agreement of monthly global and local CO_2 mole fraction (ppm) and its G_{ATM} (ppm yr^{-1}) across various networks and methodologies (see Table 1 and Fig. 4) for the period 2001-2020. Panel (a) presents the Mean Error (ME) quantifying the difference for each pair, focusing on CO_2 mole fraction, while panel (b) does the same for G_{ATM}. The significance levels of paired t-test for ME are indicated as follows: * p<0.1, ** p<0.05, *** p<0.01. Panel (c) and (d) present the Root Mean Squared Error (RMSE) for CO_2 mole fraction and G_{ATM}, respectively. Panel (e) and (f) present the Pearson Correlation Coefficient (r) for CO_2 mole fraction and G_{ATM}, respectively.

Formatted: Space Before: 0 pt, After: Auto, Line spacing: single

Formatted: Superscript

Formatted: Font: 10 pt, Bold

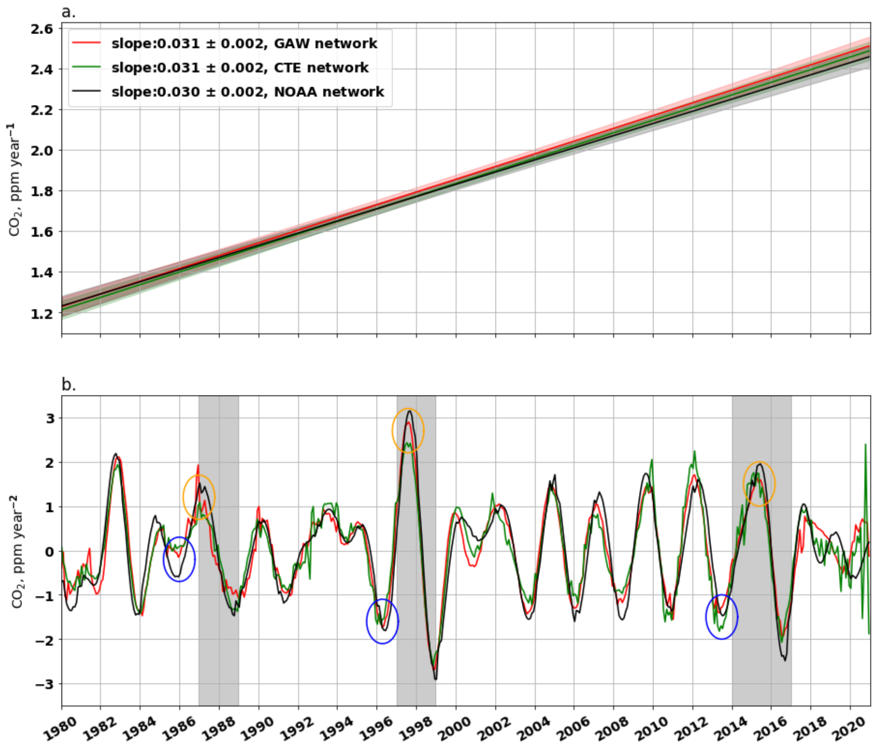

Figure ~~5~~6. Trend analysis of the global CO_2 growth rate from 1980 to 2020. Panel (a) shows the trends of CO_2 growth rate for the GAW network (red line), the CTE network (green line) and the NOAA network (black line) during the whole period 1980-2020, the CO_2 growth rate is derived from GAW (~~semi-NOAA~~GFIT), CTE_obs (~~semi-NOAA~~GFIT) and NOAA analysis (Fig. 4b~~b~~). Panel (b) shows the trend of CO_2 growth rate for each month during 1980-2020, calculated as the derivative of the growth rate. The grey bands mark the period of three strong El Niño events, i.e 1987-1988, 1997-1998 and 2014-2016.

Despite differences in the global averaged surface CO_2 mole fractions derived from different networks and analysis methods, the G_{ATM} derived from GAW network, CTE network and its model output, and NOAA network ~~agree well~~exhibits strong agreement during 1980-2020 (ME<0.031 ppm yr^{-1}, RMSE<0.217 ppm yr^{-1}, r>0.948, Fig. 4b and S1). The differences in the G_{ATM} remain below 0.023 ppm yr^{-1} during 2001-2020, with low or no significance level (Fig. 5b)~~-~~, especially when comparing the annual G_{ATM} (Fig. S2b).~~(r>0.903, RMSE<0.192 ppm yr-1, MAE<0.158 ppm yr-1, ME<0.025 ppm yr-1, Table S1) during the common period (Fig. 4b).~~ Furthermore, over the long-term period of 40 years, the estimated local growth rate at MLO (ME<0.046 ppm yr^{-1} higher, RMSE<0.272 ppm yr^{-1}, r>0.915) and SPO (ME<0.049 ppm yr^{-1} lower, RMSE<0.305 ppm yr^{-1}, r>0.888) behaves similarly to the G_{ATM} derived from GAW, CTE and NOAA network (Fig. 4b and S1). However, noticeable monthly differences between the local and global growth rates, deviating up to approximately 0.8 ppm yr^{-1}, and time shifts are observed (Fig. 4b).

The trend analysis reveals that with development of continental sites, the slope of the trend of annual global CO_2 mole fraction changes from NOAA network (1.832 ± 0.029 ppm yr^{-1}) to CTE network (1.859 ± 0.029 ppm yr^{-1}) during 1980-2020 (Fig. S4). However, ~~The trend analysis shows that~~ the G_{ATM} increased steadily at a rate of ~~(~~0.030 ± 0.002 ppm per year each year~~)~~ from 1980 to 2020 (Fig. ~~5a~~6a), based on the observations from the three networks (i.e. GAW, CTE and NOAA). ~~-~~This implies that over long-term period (here 40 years), the networks with and without continental sites ~~show~~ exhibits the same trend of the G_{ATM} and has little effect on the transient change in the rate of CO_2 increase in the atmosphere. Hence, the role of CO_2 advective

Formatted: Superscript

Formatted: Superscript

Formatted: Superscript

Formatted: Subscript

transport and mixing~~ plays a negligible role~~ in estimating the long-term change of the G_{ATM} appears negligible. However, ~~there is a clear~~a notable difference emerges in the short-term (here one month) change of the G_{ATM} between the networks with and without continental sites (Fig. ~~5b~~6b). ~~The~~ El Niño events are known to~~often~~ diminish~~es~~ net global C uptake (due to factors such as~~e.g.~~ droughts, floods and fires) ~~and~~ while increasing~~es~~ global CO_2 growth rate (Sarmiento et al., 2010). During three strong El Niño events, which are marked as grey bands in Fig. 6b, ~~The~~ the G_{ATM} derived from the GAW and CTE network (red and ~~blue~~ green lines) begins to increase~~s~~ approximately 1-2 months (Table S2) earlier before the El Niño events ~~before the three strong El Niño events~~ (marked as blue circles in Fig. ~~5b~~6b) and reaches its~~the~~ peak approximately 1-2 months (Table S2) earlier during the El Niño events (marked as orange circles in Fig. ~~5b~~6b), compared to the G_{ATM} derived from the NOAA network (black line). This ~~indicates~~ suggests that continental sites can ~~help~~ aid in the early detection of ~~the change of~~ G_{ATM} changes resulting from changes in~~which is caused by~~ biogenic emission or uptake~~ changes~~. The CTE network (green line) even detects the change~~ even~~ one month earlier than the GAW network (red line) e.g. for the ~~three~~ El Niño 1997-1998 event~~s~~ (Fig. ~~5b~~6b, Table S2)~~.~~ This earlier detection~~which~~ is attributed~~due~~ to the inclusion of even more continental sites ~~included~~ in the CTE network (Fig. 1), although the more continental sites also induce the ~~larger~~ greater variability.

Table ~~1~~ 2 ~~shows~~ presents the global annual CO_2 mole fraction and its G_{ATM} derived from GAW (~~semi-NOAA~~GFIT), ~~together~~ along with the uncertainty estimates~~d~~using~~ by~~ the bootstrap method. The global average surface CO_2 mole fraction has increased from 339.17±0.38 ppm in 1980 to 413.06±0.16 ppm in 2020~~ (Table 1, Fig. S1)~~. Notably, t~~T~~he uncertainty is greater before 1990~~, is larger than after 1990,~~ primarily due to the limited number of ~~fewer~~ measurement stations worldwide during that period~~over the globe before 1990~~. The average G_{ATM} for the two decades before 2000 is ~~about~~ approximately 1.54±0.08 ppm yr^{-1}~~.~~, H~~h~~owever, in the following two decades, it has experienced ~~-~~increases~~s~~, reaching~~ to~~ 1.91±0.05 ppm yr^{-1} during ~~(~~2000-2009~~)~~ and further rising to 2.41±0.06 ppm yr^{-1} during ~~(~~2010-2019~~)~~ (Table 2, ~~Table 1,~~ Fig. S5~~1~~).

Table ~~1~~2. Annual global averaged CO_2 mole fraction (Mean, ppm) and its G_{ATM} (ppm yr^{-1}) derived from GAW observations using ~~semi-NOAA~~GFIT method. U(Mean) and U(G_{ATM}) respectively indicate the uncertainty of Mean and its G_{ATM} as 68% confidence interval. The annual value is averaged over the monthly values of the year.

Year	**1980**	**1981**	**1982**	**1983**	**1984**	**1985**	**1986**	**1987**	**1988**	**1989**
Mean	339.17	340.16	341.03	342.59	344.46	345.69	347.08	348.99	351.45	353.15
U(Mean)	0.38	0.24	0.19	0.24	0.26	0.22	0.14	0.15	0.12	0.15
G_{ATM}	1.65	1.07	0.88	2.02	1.32	1.38	1.55	2.38	2.08	1.23
U(G_{ATM})	0.12	0.10	0.15	0.13	0.08	0.11	0.14	0.08	0.09	0.06
Year	**1990**	**1991**	**1992**	**1993**	**1994**	**1995**	**1996**	**1997**	**1998**	**1999**
Mean	354.22	355.64	356.37	357.09	358.51	360.52	362.27	363.40	366.14	368.10
U(Mean)	0.10	0.11	0.10	0.10	0.11	0.12	0.12	0.10	0.10	0.10
G_{ATM}	1.41	1.03	0.65	1.22	1.72	2.06	1.16	1.82	2.89	1.34
U(G_{ATM})	0.08	0.06	0.05	0.05	0.05	0.08	0.07	0.05	0.05	0.05
Year	**2000**	**2001**	**2002**	**2003**	**2004**	**2005**	**2006**	**2007**	**2008**	**2009**
Mean	369.30	370.77	372.92	375.45	377.22	379.28	381.38	383.20	385.26	386.78
U(Mean)	0.12	0.11	0.10	0.10	0.10	0.10	0.09	0.10	0.10	0.11
G_{ATM}	1.58	1.58	2.33	2.17	1.66	2.42	1.75	2.20	1.71	1.68
U(G_{ATM})	0.05	0.06	0.06	0.04	0.04	0.03	0.05	0.04	0.05	0.04
Year	**2010**	**2011**	**2012**	**2013**	**2014**	**2015**	**2016**	**2017**	**2018**	**2019**
Mean	389.01	390.97	393.14	396.00	397.79	400.12	403.47	405.70	407.93	410.57
U(Mean)	0.12	0.12	0.14	0.11	0.10	0.10	0.11	0.09	0.10	0.13
G_{ATM}	2.32	1.73	2.74	2.30	1.91	2.98	2.95	2.04	2.50	2.61

Formatted: Font: Bold, Font color: Auto
Formatted: Font: Bold, Font color: Auto
Formatted: Font: Bold
Formatted: Font: Bold, Font color: Auto
Formatted: Font: Bold, Font color: Auto
Formatted: Font: Bold
Formatted: Font: Bold, Font color: Auto
Formatted: Font: Bold, Font color: Auto
Formatted: Font: Bold, Font color: Auto
Formatted: Font: Bold
Formatted: Font: Bold, Font color: Auto
Formatted: Font: Bold, Font color: Auto
Formatted: Font: Bold
Formatted: Font: Bold, Font color: Auto
Formatted: Font: Bold, Font color: Auto
Formatted: Font: Bold, Font color: Auto
Formatted: Font: Bold, Font color: Auto
Formatted: Font: Bold
Formatted: Font: Bold, Font color: Auto
Formatted: Font: Bold, Font color: Auto
Formatted: Font: Bold
Formatted: Font: Bold, Font color: Auto
Formatted: Font: Bold, Font color: Auto
Formatted: Font: Bold, Font color: Auto
Formatted: Font: Bold, Font color: Auto
Formatted: Font: Bold
Formatted: Font: Bold, Font color: Auto

U(G$_{ATM}$)	0.05	0.06	0.09	0.05	0.04	0.05	0.06	0.06	0.07	0.05

Year	**2020**
Mean	413.06
U(Mean)	0.16
G$_{ATM}$	2.60
U(G$_{ATM}$)	0.16

3.2 Vertical profile of global CO_2 mole fraction

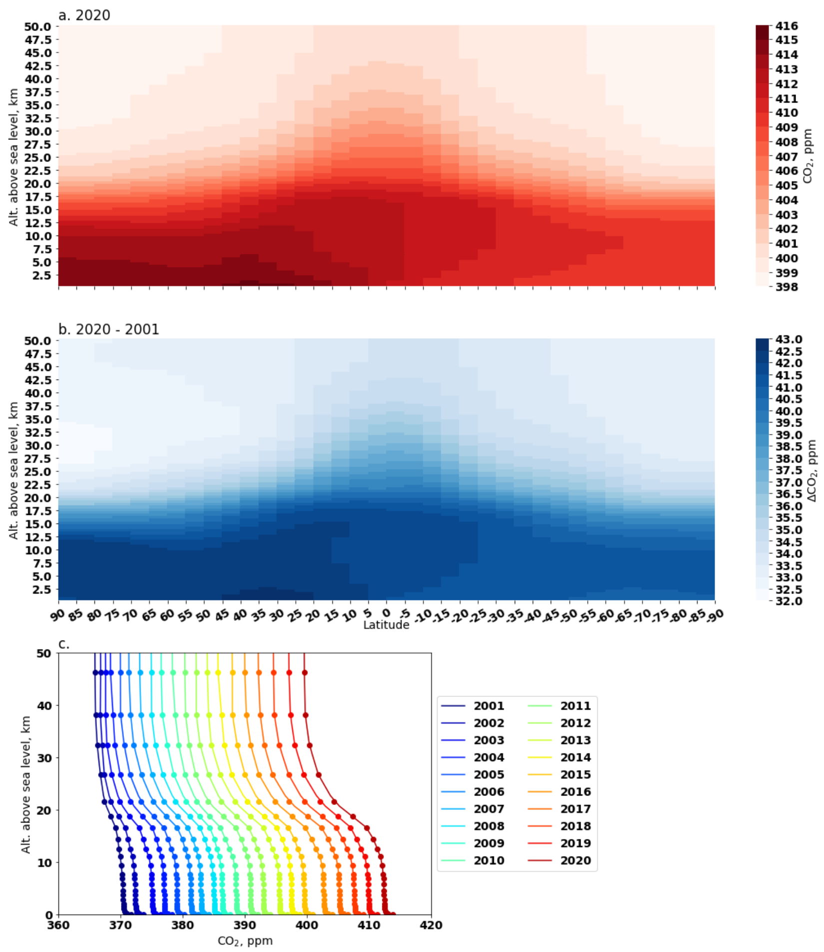

Figure ~~6~~7. Global vertical profile of CO_2 mole fraction derived from CTE model output. Panel (a) ~~shows~~ presents the vertical profile in 2020. Panel (b) present~~show~~s the difference of the vertical profile between 2001 and 2020. Panel (c) present~~show~~s the annual mean vertical profile from 2001 to 2020, the dots mark CTE vertical level heights and lines are the linear interpolation between the heights.

The CTE model simulates CO_2 mole fraction ~~over a~~on global 3D grids, ~~which allows~~enabling us to ~~view~~ visualize the modelled vertical CO_2 profile. In the lower atmosphere, highest CO_2 mole fraction ~~are~~is found in the Northern mid-latitude region (dark red between 30 °N and 40 °N, Fig. ~~6a~~7a~~),~~). This area experiences~~where~~ more anthropogenic emissions~~ take place~~, which are

Formatted: Font: Bold, Font color: Auto
Formatted: Font: Bold
Formatted: Font: Bold, Font color: Auto
Formatted: Font: Bold, Font color: Auto
Formatted: Font: Bold, Font color: Auto
Formatted: Font: Bold
Formatted: Font: Bold, Font color: Auto
Formatted: Font: Bold, Font color: Auto
Formatted: Font: Bold
Formatted: Font: Bold, Font color: Auto

subsequently transported towards both northern and southern latitudes. The latitudinal and interhemispheric gradient of atmospheric CO_2~~.~~, as shown~~found~~ in Fig. ~~6a~~7a, is influenced not only~~ determined~~ by differences in the latitudinal and interhemispheric~~ differences in~~ fossil fuel emissions and seasonal exchanges with terrestrial biota (Denning et al., 1995), but ~~is~~ also by~~ due to~~ atmospheric transport (Patra et al., 2011). ~~With~~ As ~~increasing~~ altitude increases, the gradient between the Northern and Southern hemisphere becomes small and levels out at higher altitudes (e.g. >50 km). When comparing the vertical profile change between 2001 and 2020 (Fig. ~~6b~~ 7b and ~~6c~~7c), we observe that the CO_2 mole fraction increases slowly~~er~~ in~~at~~ the higher atmosphere (>25 km altitude) ~~than~~ compared to~~the increase at~~ the lower atmosphere (<25 km altitude). Fig. ~~6c~~ 7c shows that the vertical gradient (difference between 50 km and 0.05 km) changes from ~~∼~~approximately 5 ppm in~~for~~ 2001 to around ~~∼~~13 ppm in~~for~~ 2020. The high vertical gradient in 2020 reflects the accumulation of CO_2 in the lower atmosphere, ~~which is caused by~~resulting from continuous CO_2 emissions from the surface during 2001-2020 and slow vertical transport. The low vertical gradient in 2001 is partly due to lower surface emissions.

Pressure-weighted average CO_2 mole fraction in the lower atmosphere (0 to 0.35 km altitude) and the entire atmosphere are calculated from CTE output. The annual absolute change in CO_2 mole fraction, computed as the difference between annual means, is more pronounced in the lower atmosphere (orange bars in Fig. S6a) than in the entire atmosphere (blue bars in Fig. S6a). The reason is that the entire atmosphere has a larger air volume than the lower atmosphere, and changes in the surface CO_2 sinks and sources are diluted due to atmospheric horizontal and vertical transport. The CO_2 annual absolute change derived from GAW (GFIT), GAW (WDCGG) and NOAA (represented by red, purple and brown bars in Fig S6a) shows small positive or negative differences from the CTE_output (GFIT) and CTE_global (GFIT) across different years. However, over the long term (e.g. on a decadal scale, 2001-2010 and 2011-2020), the CTE model-derived changes in lower and entire atmospheric CO_2 shows good agreement (<0.09 ppm yr^{-1}) with the surface observation-based estimate, especially for lower atmospheric CO_2 (<0.07 ppm yr^{-1}). In Fig. S6b, the interannual variability (IAV) of CO_2 mole fraction derived from CTE model follows a similar temporal pattern as the observation-based IAV derived from the GAW and NOAA network, especially the IAV of the low-level atmosphere (orange bars) exhibits strong agreement with the observation-based IAV (r>0.971, RMSE<0.178 ppm).

Formatted: Space Before: 12 pt

Formatted: Font: Italic, Pattern: Clear (White)

3.3 Relationship between the surface CO_2 mole fraction and atmospheric CO_2 mass

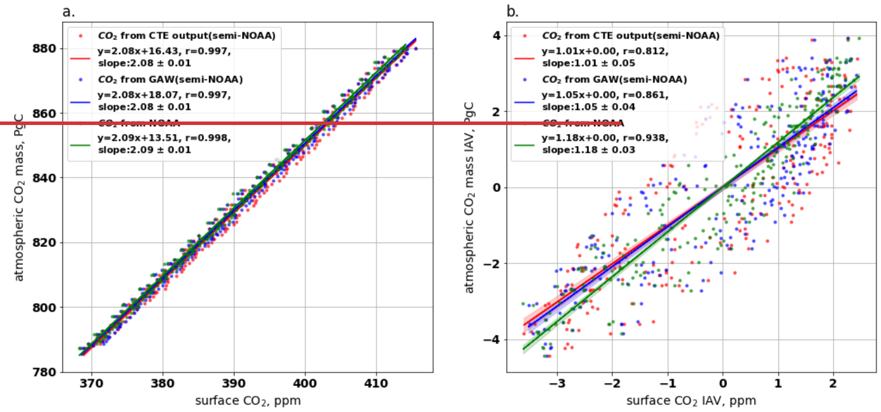

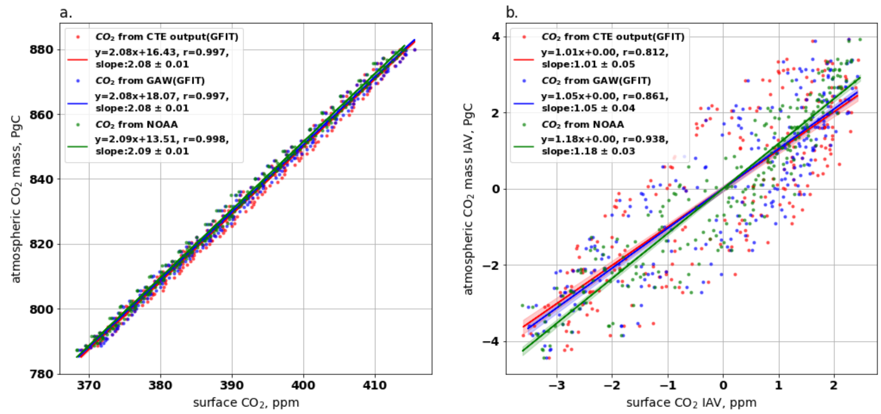

Figure ~~7~~8. Relationship between the monthly surface CO_2 mole fraction and atmospheric CO_2 mass. The atmospheric CO_2 mass calculated from the 3D CTE output. In panel (a), the monthly surface CO_2 derived from the CTE_output (~~semi-NOAA~~GFIT), GAW (~~semi-NOAA~~GFIT) and NOAA analysis, presented as blue, red and green dots, respectively. Panel (b) compares the corresponding interannual variability (IAV) of the atmospheric CO_2 mass and the surface CO_2. The IAV is calculated as the anomaly departure from a quadratic trend.

The a~~A~~tmospheric CO_2 mass, calculated from the CTE output as a function of air mass and CO_2 concentration (Text S3), has increased from 789.46 PgC in 2001 to 877.88 PgC in 2020 (Fig. ~~S3a~~S7a). The spatial distribution of the atmospheric CO_2 mass ~~can be seen~~is presented in Fig. ~~S3b~~ S7b and Fig. ~~S3c~~S7c. Monthly global surface CO_2 mole fraction derived from CTE_output (GFIT) ~~CTE output (red dots, Fig. 7a) at the 230 sites used in CTE with the semi-NOAA method (CTE_output (semi-NOAA))~~ and GAW (GFIT)~~GAW observations~~, represented as ~~(~~red and blue dots in~~,~~ Fig. ~~7a~~8a~~,)~~ ~~at 139 GAW sites with the semi-NOAA method (GAW (semi-NOAA)) has~~exhibit a similar linear relationship with the monthly atmospheric CO_2 total mass, both ~~(~~showing the same slope of 2.08±0.01 PgC ppm^{-1}~~) as the monthly atmospheric CO_2 total mass derived from the CTE output~~. Similarly, ~~The~~ NOAA CO_2 (green dots, Fig. ~~7a~~8a) also demonstrates~~shows~~ a ~~similar~~ comparable linear relationship ~~(has~~with a slope of 2.09±0.01 PgC ppm^{-1}~~)~~. Notably, t~~T~~he slope or conversion factor in Fig. ~~7a~~ 8a is slightly lower than the factor 2.12 PgC ppm^{-1} used in Ballantyne et al. (2012) for the period 1980-2010. ~~The~~ This minor~~small~~ difference in the conversion factor is expected, ~~considering~~ considering the different model and data used.

We further compare the interannual variability (IAV), calculated as the anomaly departure from a quadratic trend,~~)~~ of the atmospheric CO_2 mass and the surface CO_2 (Fig. ~~7b~~8b)~~,)~~. T~~t~~he coefficient of the linear relationship ~~is very close~~closely approaches~~ to~~ ~1.0, ~~which~~ indicating~~es~~ the temporal changes in atmospheric CO_2 mass aligns~~grees~~ with the temporal changes in surface CO_2 mole fraction. The CO_2 IAV based on the NOAA network exhibits a slightly closer relationship (r=0.938) with the CTE atmospheric CO_2 mass estimates ~~The NOAA network tracks atmospheric CO_2 change slightly better (r=0.938)~~ than the GAW (r=0.861) and CTE (r=0.812) networks~~,~~. This finding is consistent with~~given~~ the long atmospheric residence~~t~~ time and well-mixed nature of~~ atmospheric~~ CO_2~~.~~ in the NOAA network. Overall, the relationship found in Fig. ~~7~~ 8 implies that the current surface CO_2 network can effectively serve as an~~be a good~~ indicator of the CO_2 mass changes ~~in~~ throughout the ~~whole~~ entire atmosphere through a linear relationship.

Formatted: Subscript

Formatted: Subscript

~~3.4 Annual absolute change and interannual variability of global CO_2 mole fraction~~

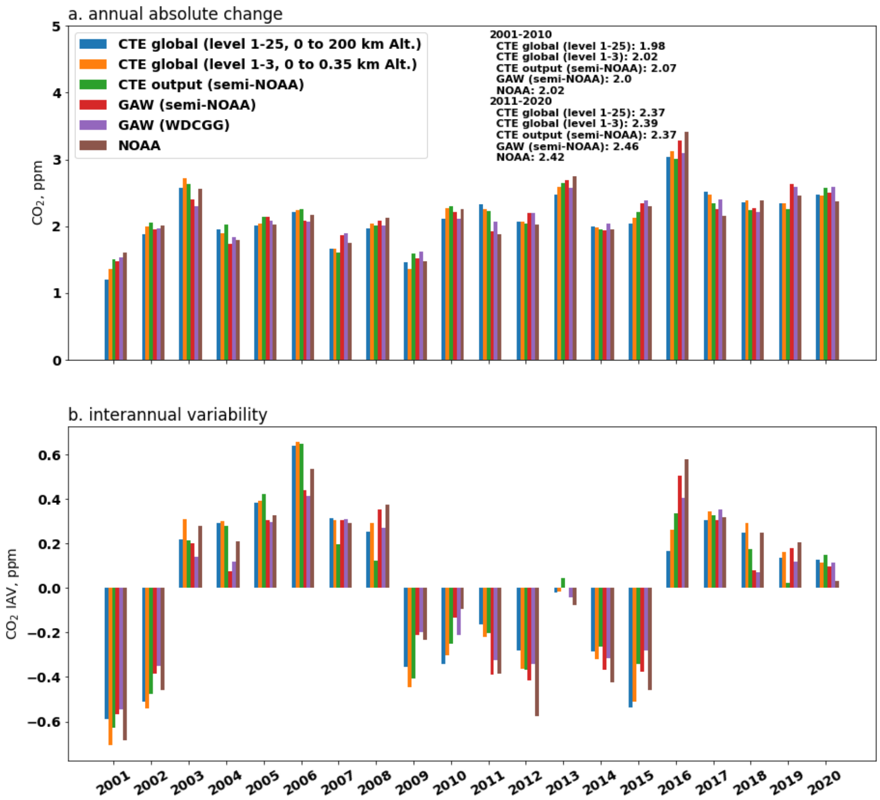

~~**Figure 8. Annual absolute change and interannual variability of global CO_2 mole fraction derived from different data (CTE model, GAW observation and NOAA observation) and analysis methods (semi-NOAA method, WDCGG method and NOAA method) for 2000-2020. Panel (a) shows the annual absolute change which is the difference between annal mean. Averages over 2001-2010 and 2011-2020 are also shown. Panel (b) shows the IAV which is calculated as the anomaly departure from a quadratic trend.**~~

~~Pressure-weighted average CO_2 in the lower atmosphere and whole atmosphere is derived from CTE output. The annual absolute change (calculated as the difference between annual mean) of CO_2 in the lower atmosphere (0 to 0.35 km altitude, orange bars in Fig. 8a) is more sensitive to surface sink and source than the change in the whole atmosphere (blue bars). The reason is that the whole atmosphere has a larger air volume than the lower atmosphere, and the change of the surface CO_2 is~~

~~diluted due to horizontal and vertical transport. The CO_2 change derived from the observations of the GAW network (red bars for semi-NOAA method, purple bars for WDCGG method) and the NOAA network (brown bars), shows a small positive or negative difference from the CTE results over the different years. However, over the long term (e.g. decadal scale, 2001-2010 and 2011-2020), the CTE model derived change of lower and whole atmospheric CO_2 shows good agreement (<0.09 ppm yr^{-1}) with the surface observation-based estimate, especially for the lower atmospheric CO_2 (<0.07 ppm yr^{-1}). Fig. 8b shows the IVA derived from CTE (blue, orange and green bars) follows a similar temporal pattern as the observation-based IVA derived from the GAW and NOAA network (red, purple and brown bars), especially the IVA of the low-level atmosphere (orange bars) show good agreement with the observation-based IVA (r>0.971, RMSE<0.178 ppm).~~

4 Discussion

~~During~~ Over the past few decades, observational networks have been extended ~~(e.g.~~beyond ~~from~~ the NOAA MBL network~~)~~ to include ~~the~~ more continental sites,~~s~~ such as in the~~(e.g.~~ GAW ~~network~~ and CTE networks~~,~~ (Fig. 1). These expansions aim ~~in order~~ to better monitor global CO_2 concentrations and quantify CO_2 sources and sinks. ~~Although~~ While the continental observations encompass~~include~~ contributions from both substantial~~big~~ sources of anthropogenic emissions and ~~big~~ sources/sinks from terrestrial vegetation ~~off/during the growing season~~and soil, these continental observations ~~show~~ consistently yield a~~n overall~~ higher global surface CO_2 mole fraction in the overall global CO_2 analysis, ~~which~~ indicating~~es~~ that they are influenced by a bigger net source. We find that the global mean derived from the GAW network is consistently ~~on average~~ 0.329 (~~semi-NOAA~~GFIT method) or 0.~~336~~ 335 (WDCGG method) ppm ~~consistently~~ higher than that derived from the NOAA network during 1980-2020~~,~~. S~~s~~imilarly, Tsutsumi et al. (2009) reported a roughly ~~∼~~0.350 ppm higher mole fraction in the GAW network ~~was found in Tsutsumi et al. (2009)~~ for years 1983-2006. Notably, t~~T~~he CTE network ~~even~~ leads to an even higher global mean (0.422 ppm during 1980-2020), which is likely due to more observational sites locate in the Northern Hemisphere, where the highest anthropogenic emissions ~~take place~~occur. This also explains the large fluctuation of CO_2 concentrations observed during the winters and summers during 2001-2020 (~~green and orange lines,~~ Fig. 4a~~a~~). In the future, with the ~~we expect that~~ addition of~~ing~~ new observation sites, ~~(~~particularly~~specially~~ in the Northern Hemisphere,~~)~~ ~~in~~to the existing~~current~~ observational network (e.g. GAW network), we ~~would~~ expect that this would lead to higher global surface CO_2 levels and a greater~~larger~~ amplitude in~~of~~ the global CO_2 seasonal cycle in the global CO_2 analysis.

Although Friedlingstein et al. (2022) reported a 5.4% drop (~0.52 PgC) in fossil fuel CO_2 emissions in 2020 (due to restrictions on e.g. transport, industry, power etc during the COVID-19 pandemic), the increase in annual CO_2 from 2019 to 2020 (2.60±0.16 ppm yr^{-1}) remains at a similar level as from 2018 to 2019 (2.61±0.05 ppm yr^{-1}). In principle, an equivalent drop of roughly 0.25 ppm yr^{-1} (according to the conversion factor 2.08 PgC ppm^{-1} in Fig. ~~7a~~8a) or roughly 0.13 ppm yr^{-1} (according to the annual absolute change, red bars in Fig. S6~~8~~a) in the growth rate should be visible for period 2019-2020 due to the declined CO_2 emissions. However, such a short-term human activity induced change ~~of~~ in the CO_2 growth rate may be hidden by the natural variability. The bootstrap analysis is used in this study (also in Conway et al., (1994) and Tsutsumi et al., (2009)) to estimate the uncertainty of the CO_2 temporal mean and its growth rate and to assess how sensitive the global value is to the distribution of sampling sites. The relatively large uncertainty (±0.16 ppm yr^{-1}) at the end of 2020 compared to previous years (Table ~~1~~2) is likely due to an end-effect associated with the curve fitting and filter procedure. The end-effect is a tendency for the growth rate to ~~turn~~ converge toward the mean value at the end of the record (Conway et al., 1994).~~,~~ T~~t~~herefore, Conway et al. (1994) suggested that ~~the last 6 months of~~ the growth rate curves for the last 6 months should be viewed with caution. Reducing the end-effect requires further study, such as using machine learning or bias-correction methods to extrapolate the smoothed trend for a short period (e.g. one year) before and after. This extrapolated portion is used exclusively for calculating local mole fraction and growth rate, while it is not included in the global or zonal average, as it could introduce additional uncertainty.

Formatted: Font color: Auto

Extrapolation beyond the measurement period extends knowledge gained from a limited period of measurements. During a limited measurement period, we can define the average seasonality, long-term trend, and short-term variation at a measurement site. The long-term trend of an individual site can be extrapolated by various methods, such as referring to the latitude reference time series (Masarie and Tans, 1995) or calculating the mean long-term trend over sites within a certain latitudinal zone (e.g. 30°) (Tsutsumi et al., 2009). This extrapolated trend is then combined with the average seasonality to produce estimates beyond the measurement period. However, the extrapolation process relies on the assumption that the relationship of an individual site to the latitude reference remains invariant in time, while in reality the relationship between nearby sites is continuously changing (Masarie and Tans, 1995). In addition, the short-term variation is often ignored or estimated from nearby sites, introducing extra uncertainty into the extrapolation process. In this study, we find that the WDCGG method with extrapolation (GAW (WDCGG+)) results in a global surface CO_2 mole fraction approximately 0.096 ppm higher than the WDCGG method without extrapolation (GAW (WDCGG)) using the same GAW observations, although the extrapolation has a minor effect on the growth rate (Table S1). Therefore, we chose not to use extrapolation beyond the measurement period in our analysis. As the number of long-term measurements increases, the need for such extrapolation becomes less necessary.

Formatted: Font: (Default) Times New Roman, 10 pt, (Asian) Chinese (Simplified, Mainland China)

Our analysis shows that basing the CO_2 growth rate on GAW surface observations does not introduce a large bias (with an~~on~~ average agreement within 0.~~015~~ 016 ppm yr^{-1}) compared to a full atmospheric analysis (Fig. 4b~~b~~ and 58~~, Table S1e-f~~). This full atmosphere CO_2 was provided by the CTE model, in which the global annual mean CO_2 is significantly overestimated compared to GAW observations (e.g. 0.299 ppm higher in CTE_output (GFIT~~semi-NOA~~), or 0.186 ppm higher in the CTE_global (~~semi-NOAA~~GFIT) during 2001-2020). The overestimate derived from the CTE_output (~~semi-NOAA~~GFIT)~~, i.e. CTE outputs at the CTE 230 sites,~~ is mainly due to more sites in the Northern Hemisphere in the CTE network than in the GAW network. The lower overestimate derived from the CTE_global (~~semi-NOAA~~GFIT)~~, i.e. CTE outputs at full global grids at the low-level atmosphere,~~ implies that the biases in CTE outputs are not uniform spatially and ~~attempt~~ tend to balance out. We estimate the CTE bias by comparing the observations and CTE outputs at the same sites, which results in a 0.069 ppm low bias derived from the CTE outputs in calculating the global surface CO_2 mole fraction.

The local growth rate at MLO and SPO generally behaves similarly to the global growth rate derived from the GAW, CTE, and NOAA networks (Fig. 4b and S1). However, the local CO_2 mole fraction and its seasonal cycle noticeably differ from global estimates derived from different observational networks. In this regard, the utilization of individual sites for the evaluation of the global average mole fraction and its growth rate is not precise and can only be used for illustration rather than as a substitute for the proper global average calculation. The local observation sites, often situated away from significant local sources and sinks, such as MLO, provide long-term and high-quality data, serving as reference data for global CO_2 mole fraction. However, a single observation site cannot capture the CO_2 spatial variability, transport, and mixing. To overcome these limitations, global CO_2 trends and variations are best assessed by integrating data from multiple sources and locations.

Formatted: (Asian) Chinese (Simplified, Mainland China)

Different observational networks (i.e. NOAA network, GAW network and CTE network) are analysed in this study, ~~which~~ revealing~~shows a~~ differences in calculated global surface CO_2 mole fractions equivalent to the current atmospheric growth rate over a three-month period. This ~~implies~~ suggests that the station selection, especially if and how many continental observations are used, has some influence on ~~but not a particularly strong influence on~~ the derived global surface CO_2 levels, but it is not particularly strong. Nowadays, ~~more and more~~an increasing number of continental observations are established~~ in order~~ to monitor biogenic sources and sinks, ~~and~~ providing further ~~provide~~ insight into the climate change and the associated ecosystem processes (Ciais et al., 2005, Ramonet et al., 2020). Such continental observations carry more variability in measurements than the marine observations, which ~~needs~~ requires~~some~~ caution when including~~used~~ them in the mix of stations used to~~for~~ determine~~ing~~ global surface CO_2 mole fraction. O~~However, o~~ur study ~~shows~~ demonstrates that continental sites can help early detect ~~the~~ changes in~~of~~ CO_2 growth rate caused by biogenic emission change, such as those resulting from~~(e.g. caused by~~ El Niño events~~)~~. ~~Besides~~Furthermore, the current observational networks (with and without continental sites) and CTE model show a good agreement ~~within 0.025 ppm yr^{-1}~~ on the global CO_2 growth rate, with low or no significant differences within

0.023 ppm yr^{-1} ~~over long-term period~~during 2001-2020 and 0.031 ppm yr^{-1} during 1980-2020. This implies that the current observation networks (~~e.g.~~ as shown in Fig. 1, represent for ~~multiple~~ various ecosystems, ~~multiple~~ sinks, ~~and~~ sources, and ~~different~~ latitudes) have a similar good capacity to capture changes in the global surface CO_2 ~~changes.~~, ~~a~~although there is the spatial and temporal variability ~~of~~ in the CO_2 growth rate (e.g. Conway et al. 1994).

We also notice that the uncertainty in global CO_2 growth rate is approximately 0.07 ppm yr^{-1}, as derived from GAW (~~semi-NOAA~~GFIT) and averaged over 1980-2020 (Table ~~1~~2). ~~In order t~~ To reduce the uncertainty to 0.02 ppm yr^{-1} (equivalent to 1% of the global CO_2 growth rate)~~o reduce this uncertainty~~, ~~we recommend~~in principle it would theoretically requires adding more stations to the current observation network. We conducted an experiment ~~(Fig. S4) which~~that demonstrates how~~that~~ the uncertainty of the global CO_2 growth rate exponentially increases as the number of land observation sites decreased~~is reduced~~ (Fig. S8). According to our experiment, ~~To reduce the uncertainty to 0.02 ppm yr^{-1} (equivalent to 1% of the global CO_2 growth rate),~~ to achieve the goal of reducing the uncertainty to 0.02 ppm yr^{-1}, ~~our experiment indicates that~~ 332 land observation sites are required ~~required~~ (Fig. ~~S4~~S8). However, the required number of sites also depends on their measurement accuracy, consistency, and geographical distribution (i.e. CO_2 footprint coverage of observation network, and the importance of the network design was addressed by Storm et al. (2022))~~, measurement accuracy, and consistency~~.

~~Extrapolation beyond the measurement period extends knowledge gained from a limited period of measurements. During a limited period of measurement, we can define the average seasonality, long-term trend, and short-term variation at a measurement site. The long-term trend of individual site is extrapolated, for example by referring to the latitude reference time series (Masarie and Tans, 1995) or the mean long-term trend over sites within a certain (e.g. 30°) latitudinal zone (Tsutsumi et al., 2009), and then combining the extrapolated trend with average seasonality to produce the estimate beyond measurement period. The extrapolation requires the assumption that the relationship of an individual site to the latitude reference is invariant in time, however, the relationship between nearby sites is continuously changing (Masarie and Tans, 1995). Besides, the short-term variation is ignored or estimated from nearby sites, which introduces extra uncertainty from extrapolation. In this study, we find that the WDCGG method with extrapolation (GAW (WDCGG+)) results in ~0.096 ppm higher in the global surface CO_2 mole fraction than the WDCGG method without extrapolation (GAW (WDCGG)) using the same GAW observations, although the extrapolation has a tiny effect on the growth rate (Table S2). Therefore, extrapolation beyond the measurement period is not used in our analysis. With the increasing number of long-term measurements, this extrapolation becomes less and less necessary.~~

5 Conclusions

The WMO GAW ~~Global Atmosphere Watch~~ CO_2 network documents the gradual global accumulation of CO_2 in the atmosphere due to human activities.~~,~~ I~~and~~t has been used to assess the large-scale and long-term environmental consequence of fossil CO_2 emission and land use changes. The high-quality observations conducted by the WMO GAW network include not only background stations (most of NOAA MBL stations) but also continental stations. This comprehensive network enables proper global average calculation. Furthermore, the WMO has initiated a new program, Global Greenhouse Gas Watch (GGGW), with the aim of establishing a reference network. This network will be built on the high-quality observations already performed under the WMO GAW program that follows consistent good practices and standards. Although the current monitoring networks have limitations in terms of geographical coverage, data consistency, and long-term measurements, they are well-equipped and have the capacity to effectively represent global surface CO_2 mole fraction and its growth rate and trends in atmospheric CO_2 mass changes. The three different analysis methods yield very similar global CO_2 increases from 2001 to 2020, which gives confidence in using any one of them in climate change studies. ~~Although the current CO_2 network is sparse due to operational costs and logistical constraints, it has a good capacity to represent global surface CO_2 mole fraction~~

~~and its growth rate and trends in atmospheric CO_2 mass changes. The three different analysis methods yield very similar global CO_2 increase from 2001 to 2020, which gives confidence to use either one of them in climate change study. The c~~Continuous monitoring ~~the~~ of atmospheric CO_2, ~~basing~~ based on the current GAW network together with reliable global data integration methods, provides essential information. This includes understanding trends in atmospheric CO_2 concentration, assessing the impacts of past policies, identifying high-emission areas, informing climate models, forecasting future scenarios, and raising public awareness. P~~for p~~olicymakers can rely on this information to support their efforts in mitigating the global warming. ~~Although the current CO_2 network is sparse due to operational costs and logistical constraints, it has a good capacity to represent global surface CO_2 mole fraction and its growth rate and trends in atmospheric CO_2 mass changes.~~

Formatted: Subscript

6 Data and Code Availability

All data and code necessary to calculate the global mean surface CO_2 mole fraction and Atmospheric CO_2 mass is freely available from ICOS Carbon Portal [https://doi.org/10.18160/Q788-9081]. The file list of results and code can be found in Text S4.

Acknowledgments

We acknowledge Ingrid Luijkx for providing the TM5 data, WMO GAW Principal Investigators of the WMO GAW station network for providing the observational data, Ed Dlugokencky for providing NOAA data and comments. Thanks to the support from ICOS, GAW, NOAA and CTE group.

Author Contributions

A.V. and Z.W. designed this study in discussion with Y.S., O.T and U.K..

Z.W. performed analysis and led the writing.

Y.S., Y.N. and A.O. provided the GAW data, and commented on the manuscript.

W.P. and R.K. provided CTE model results and relevant ObsPack data, and commented on the manuscript.

X.L. provided NOAA data and commented on the manuscript.

All authors contributed to the writing of the paper and interpretation of the results.

Competing Interests

The authors declare no competing interests.

Financial support

This research is a part of ICOS core work, there is no grant reference no.

References

~~BALLANTYNE, A. Á., ALDEN, C. Á., MILLER, J. Á., TANS, P. Á. & WHITE, J. 2012. Increase in observed net carbon dioxide uptake by land and oceans during the past 50 years. *Nature*, 488, 70-72. https://doi.org/10.1038/nature11299~~

~~CIAIS, P., REICHSTEIN, M., VIOVY, N., GRANIER, A., OGÉE, J., ALLARD, V., AUBINET, M., BUCHMANN, N., BERNHOFER, C. & CARRARA, A. 2005. Europe-wide reduction in primary productivity caused by the heat and drought in 2003. *Nature*, 437, 529-533. https://doi.org/10.1038/nature03972~~

~~CONWAY, T. J., TANS, P. P., WATERMAN, L. S., THONING, K. W., KITZIS, D. R., MASARIE, K. A. & ZHANG, N. 1994. Evidence for interannual variability of the carbon cycle from the National Oceanic and Atmospheric Administration/Climate Monitoring and Diagnostics Laboratory global air sampling network. *Journal of Geophysical Research: Atmospheres,* 99**,** 22831-22855. https://doi.org/10.1029/94JD01951~~

~~DENNING, A. S., FUNG, I. Y. & RANDALL, D. 1995. Latitudinal gradient of atmospheric CO2 due to seasonal exchange with land biota. *Nature,* 376**,** 240-243. https://doi.org/10.1038/376240a0~~

~~EYRING, V., GILLETT, K., ACHUTA RAO, R., BARIMALALA, M., BARREIRO PARRILLO, N., BELLOUIN, C., CASSOU, P., DURACK, Y., KOSAKA, S. & MCGREGOR, S. 2021. Human Influence on the Climate System. *Climate Change 2021: The Physical Science Basis. Contribution of Working Group I to the Sixth Assessment Report of the Intergovernmental Panel on Climate Change*. https://www.ipcc.ch/report/ar6/wg1/~~

~~FRIEDLINGSTEIN, P., JONES, M. W., O'SULLIVAN, M., ANDREW, R. M., BAKKER, D. C., HAUCK, J., LE QUÉRÉ, C., PETERS, G. P., PETERS, W. & PONGRATZ, J. 2022. Global carbon budget 2021. *Earth System Science Data,* 14**,** 1917-2005. https://doi.org/10.5194/essd-14-1917-2022~~

~~GULEV, S., THORNE, P., AHN, J., DENTENER, F., DOMINGUES, C. M., GONG, S. G. D., KAUFMAN, D., NNAMCHI, H., RIVERA, J. & SATHYENDRANATH, S. 2021. Changing state of the climate system. *Climate Change 2021: The Physical Science Basis. Contribution of Working Group I to the Sixth Assessment Report of the Intergovernmental Panel on Climate Change*. https://www.ipcc.ch/report/ar6/wg1/~~

~~HALL, B. D., CROTWELL, A. M., KITZIS, D. R., MEFFORD, T., MILLER, B. R., SCHIBIG, M. F. & TANS, P. P. 2021. Revision of the World Meteorological Organization Global Atmosphere Watch (WMO/GAW) CO 2 calibration scale. *Atmospheric Measurement Techniques,* 14**,** 3015-3032. https://doi.org/10.5194/amt-14-3015-2021~~

~~SCHULDT, K.N., et al. 2022. Multi-laboratory compilation of atmospheric carbon dioxide data for the period 1957-2021. *NOAA Earth System Research Laboratory, Global Monitoring Laboratory*. http://doi.org/10.25925/20220808~~

~~KROL, M., DE BRUINE, M., KILLAARS, L., OUWERSLOOT, H., POZZER, A., YIN, Y., CHEVALLIER, F., BOUSQUET, P., PATRA, P. & BELIKOV, D. 2018. Age of air as a diagnostic for transport timescales in global models. *Geoscientific Model Development,* 11**,** 3109-3130. https://doi.org/10.5194/gmd-11-3109-2018~~

~~KROL, M., HOUWELING, S., BREGMAN, B., VAN DEN BROEK, M., SEGERS, A., VAN VELTHOVEN, P., PETERS, W., DENTENER, F. & BERGAMASCHI, P. 2005. The two-way nested global chemistry-transport zoom model TM5: algorithm and applications. *Atmospheric Chemistry and Physics,* 5**,** 417-432. https://doi.org/10.5194/acp-5-417-2005~~

~~LÜTHI, D., LE FLOCH, M., BEREITER, B., BLUNIER, T., BARNOLA, J. M., SIEGENTHALER, U., RAYNAUD, D., JOUZEL, J., FISCHER, H. & KAWAMURA, K. 2008. High-resolution carbon dioxide concentration record 650,000–800,000 years before present. *nature,* 453**,** 379-382. http://doi.org/10.1038/nature06949~~

~~MASARIE, K. A. & TANS, P. P. 1995. Extension and integration of atmospheric carbon dioxide data into a globally consistent measurement record. *Journal of Geophysical Research: Atmospheres,* 100**,** 11593-11610. https://doi.org/10.1029/95JD00859~~

~~PATRA, P. K., HOUWELING, S., KROL, M., BOUSQUET, P., BELIKOV, D., BERGMANN, D., BIAN, H., CAMERON-SMITH, P., CHIPPERFIELD, M. P. & CORBIN, K. 2011. TransCom model simulations of CH 4 and related species: linking transport, surface flux and chemical loss with CH 4 variability in the troposphere and lower stratosphere. *Atmospheric Chemistry and Physics,* 11**,** 12813-12837. https://doi.org/10.5194/acp-11-12813-2011~~

~~PETERS, W., KROL, M., DLUGOKENCKY, E., DENTENER, F., BERGAMASCHI, P., DUTTON, G., VELTHOVEN, P. V., MILLER, J., BRUHWILER, L. & TANS, P. 2004. Toward regional-scale modeling using the two-way nested global model TM5: Characterization of transport using SF6. *Journal of Geophysical Research: Atmospheres,* 109. https://doi.org/10.1029/2004JD005020~~

~~PRESS, W. H., TEUKOLSKY, S. A., VETTERLING, W. T. & FLANNERY, B. P. 1988. *Numerical recipes in C 1st edition: The art of scientific computing*, Cambridge university press. https://citeseerx.ist.psu.edu/document?repid=rep1&type=pdf&doi=e05e217a58481314e070b6c8899791faa91a3e27~~

~~RAMONET, M., CIAIS, P., APADULA, F., BARTYZEL, J., BASTOS, A., BERGAMASCHI, P., BLANC, P., BRUNNER, D., CARACCIOLO DI TORCHIAROLO, L. & CALZOLARI, F. 2020. The fingerprint of the summer 2018 drought in Europe on ground-based atmospheric CO2 measurements. *Philosophical Transactions of the Royal Society B,* 375**,** 20190513. https://doi.org/10.1098/rstb.2019.0513~~

~~SARMIENTO, J. L., GLOOR, M., GRUBER, N., BEAULIEU, C., JACOBSON, A. R., MIKALOFF FLETCHER, S. E., PACALA, S. & RODGERS, K. 2010. Trends and regional distributions of land and ocean carbon sinks. *Biogeosciences,* 7**,** 2351-2367. https://doi.org/10.5194/bg-7-2351-2010~~

~~STORM, I., KARSTENS, U., D'ONOFRIO, C., VERMEULEN, A. & PETERS, W. 2022. A view of the European carbon flux landscape through the lens of the ICOS atmospheric observation network. *Atmospheric Chemistry and Physics Discussions***,** 1-25. https://doi.org/10.5194/acp-23-4993-2023~~

~~TANS, P. P., THONING, K. W., ELLIOTT, W. P. & CONWAY, T. J. 1990. Error estimates of background atmospheric CO2 patterns from weekly flask samples. *Journal of Geophysical Research: Atmospheres,* 95**,** 14063-14070. https://doi.org/10.1029/JD095iD09p14063~~

~~THONING, K. W., TANS, P. P. & KOMHYR, W. D. 1989. Atmospheric carbon dioxide at Mauna Loa Observatory: 2. Analysis of the NOAA GMCC data, 1974–1985. *Journal of Geophysical Research: Atmospheres,* 94**,** 8549-8565. https://doi.org/10.1029/JD094iD06p08549~~

~~TSUTSUMI, Y., MORI, K., HIRAHARA, T., IKEGAMI, M. & CONWAY, T. J. 2009. Technical Report of Global Analysis Method for Major Greenhouse Gases by the World Data Center for Greenhouse Gases (WMO/TD-No. 1473). *GAW Report No. 184. Geneva, WMO*,, 1-23. https://library.wmo.int/index.php?lvl=notice_display&id=12631~~

~~VAN DER LAAN-LUIJKX, I. T., VAN DER VELDE, I. R., VAN DER VEEN, E., TSURUTA, A., STANISLAWSKA, K., BABENHAUSERHEIDE, A., ZHANG, H. F., LIU, Y., HE, W. & CHEN, H. 2017. The CarbonTracker Data Assimilation Shell (CTDAS) v1. 0: implementation and global carbon balance 2001–2015. *Geoscientific Model Development,* 10, 2785-2800. https://doi.org/10.5194/gmd-10-2785-2017~~

~~WMO, G. 2022. The state of greenhouse gases in the atmosphere based on global observations through 2021. *WMO Greenhouse Gas Bulletin*. https://library.wmo.int/doc_num.php?explnum_id=11352~~

Ballantyne, A. á., Alden, C. á., Miller, J. á., Tans, P. á. & White, J. 2012. Increase in observed net carbon dioxide uptake by land and oceans during the past 50 years. *Nature,* 488**,** 70-72. https://doi.org/10.1038/nature11299

Ciais, P., Reichstein, M., Viovy, N., Granier, A., Ogée, J., Allard, V., Aubinet, M., Buchmann, N., Bernhofer, C. & Carrara, A. 2005. Europe-wide reduction in primary productivity caused by the heat and drought in 2003. *Nature,* 437**,** 529-533. https://doi.org/10.1038/nature03972

Conway, T. J., Tans, P. P., Waterman, L. S., Thoning, K. W., Kitzis, D. R., Masarie, K. A. & Zhang, N. 1994. Evidence for interannual variability of the carbon cycle from the National Oceanic and Atmospheric Administration/Climate Monitoring and Diagnostics Laboratory global air sampling network. *Journal of Geophysical Research: Atmospheres,* 99**,** 22831-22855. https://doi.org/10.1029/94JD01951

Denning, A. S., Fung, I. Y. & Randall, D. 1995. Latitudinal gradient of atmospheric CO2 due to seasonal exchange with land biota. *Nature,* 376**,** 240-243. https://doi.org/10.1038/376240a0

Eyring, V., Gillett, K., Achuta Rao, R., Barimalala, M., Barreiro Parrillo, N., Bellouin, C., Cassou, P., Durack, Y., Kosaka, S. & Mcgregor, S. 2021. Human Influence on the Climate System. *Climate Change 2021: The Physical Science Basis. Contribution of Working Group I to the Sixth Assessment Report of the Intergovernmental Panel on Climate Change*. https://www.ipcc.ch/report/ar6/wg1/

Friedlingstein, P., Jones, M. W., O'sullivan, M., Andrew, R. M., Bakker, D. C., Hauck, J., Le Quéré, C., Peters, G. P., Peters, W. & Pongratz, J. 2022. Global carbon budget 2021. *Earth System Science Data,* 14**,** 1917-2005. https://doi.org/10.5194/essd-14-1917-2022

Gulev, S., Thorne, P., Ahn, J., Dentener, F., Domingues, C. M., Gong, S. G. D., Kaufman, D., Nnamchi, H., Rivera, J. & Sathyendranath, S. 2021. Changing state of the climate system. *Climate Change 2021: The Physical Science Basis. Contribution of Working Group I to the Sixth Assessment Report of the Intergovernmental Panel on Climate Change*. https://www.ipcc.ch/report/ar6/wg1/

Hall, B. D., Crotwell, A. M., Kitzis, D. R., Mefford, T., Miller, B. R., Schibig, M. F. & Tans, P. P. 2021. Revision of the World Meteorological Organization Global Atmosphere Watch (WMO/GAW) CO 2 calibration scale. *Atmospheric Measurement Techniques,* 14**,** 3015-3032. https://doi.org/10.5194/amt-14-3015-2021

Krol, M., De Bruine, M., Killaars, L., Ouwersloot, H., Pozzer, A., Yin, Y., Chevallier, F., Bousquet, P., Patra, P. & Belikov, D. 2018. Age of air as a diagnostic for transport timescales in global models. *Geoscientific Model Development,* 11**,** 3109-3130. https://doi.org/10.5194/gmd-11-3109-2018

Krol, M., Houweling, S., Bregman, B., Van Den Broek, M., Segers, A., Van Velthoven, P., Peters, W., Dentener, F. & Bergamaschi, P. 2005. The two-way nested global chemistry-transport zoom model TM5: algorithm and applications. *Atmospheric Chemistry and Physics,* 5**,** 417-432. https://doi.org/10.5194/acp-5-417-2005

Lüthi, D., Le Floch, M., Bereiter, B., Blunier, T., Barnola, J.-M., Siegenthaler, U., Raynaud, D., Jouzel, J., Fischer, H. & Kawamura, K. 2008. High-resolution carbon dioxide concentration record 650,000–800,000 years before present. *nature,* 453**,** 379-382. http://doi.org/10.1038/nature06949

Masarie, K. A. & Tans, P. P. 1995. Extension and integration of atmospheric carbon dioxide data into a globally consistent measurement record. *Journal of Geophysical Research: Atmospheres,* 100**,** 11593-11610. https://doi.org/10.1029/95JD00859

Patra, P. K., Houweling, S., Krol, M., Bousquet, P., Belikov, D., Bergmann, D., Bian, H., Cameron-Smith, P., Chipperfield, M. P. & Corbin, K. 2011. TransCom model simulations of CH 4 and related species: linking transport, surface flux and chemical loss with CH 4 variability in the troposphere and lower stratosphere. *Atmospheric Chemistry and Physics,* 11**,** 12813-12837. https://doi.org/10.5194/acp-11-12813-2011

Peters, W., Krol, M., Dlugokencky, E., Dentener, F., Bergamaschi, P., Dutton, G., Velthoven, P. V., Miller, J., Bruhwiler, L. & Tans, P. 2004. Toward regional-scale modeling using the two-way nested global model TM5: Characterization of transport using SF6. *Journal of Geophysical Research: Atmospheres,* 109. https://doi.org/10.1029/2004JD005020

Press, W. H., Teukolsky, S. A., Vetterling, W. T. & Flannery, B. P. 1988. *Numerical recipes in C 1st edition: The art of scientific computing*, Cambridge university press. https://citeseerx.ist.psu.edu/document?repid=rep1&type=pdf&doi=e05e217a58481314e070b6c8899791faa91a3e27

Ramonet, M., Ciais, P., Apadula, F., Bartyzel, J., Bastos, A., Bergamaschi, P., Blanc, P., Brunner, D., Caracciolo Di Torchiarolo, L. & Calzolari, F. 2020. The fingerprint of the summer 2018 drought in Europe on ground-based atmospheric CO2 measurements. *Philosophical Transactions of the Royal Society B,* 375**,** 20190513. https://doi.org/10.1098/rstb.2019.0513

Sarmiento, J. L., Gloor, M., Gruber, N., Beaulieu, C., Jacobson, A. R., Mikaloff Fletcher, S. E., Pacala, S. & Rodgers, K. 2010. Trends and regional distributions of land and ocean carbon sinks. *Biogeosciences,* 7**,** 2351-2367. https://doi.org/10.5194/bg-7-2351-2010

Schuldt, K., Mund, J. & Luijkx, I. 2022. Multi-laboratory compilation of atmospheric carbon dioxide data for the period 1957–2021; obspack_co2_1_GLOBALVIEWplus_v8. 0_2022-08-27, NOAA Global Monitoring Laboratory [data set]. *NOAA Global Monitoring Laboratory [data set],* 10**,** 20220808. http://doi.org/10.25925/20220808

Tans, P. P., Thoning, K. W., Elliott, W. P. & Conway, T. J. 1990. Error estimates of background atmospheric CO2 patterns from weekly flask samples. *Journal of Geophysical Research: Atmospheres,* 95**,** 14063-14070. https://doi.org/10.1029/JD095iD09p14063

Thoning, K. W., Tans, P. P. & Komhyr, W. D. 1989. Atmospheric carbon dioxide at Mauna Loa Observatory: 2. Analysis of the NOAA GMCC data, 1974–1985. *Journal of Geophysical Research: Atmospheres,* 94**,** 8549-8565. https://doi.org/10.1029/JD094iD06p08549

Tsutsumi, Y., Mori, K., Hirahara, T., Ikegami, M. & Conway, T. J. 2009. Technical Report of Global Analysis Method for Major Greenhouse Gases by the World Data Center for Greenhouse Gases (WMO/TD-No. 1473). *GAW Report No. 184. Geneva, WMO,***,** 1-23. https://library.wmo.int/index.php?lvl=notice_display&id=12631

van der Laan-Luijkx, I. T., Van Der Velde, I. R., Van Der Veen, E., Tsuruta, A., Stanislawska, K., Babenhauserheide, A., Zhang, H. F., Liu, Y., He, W. & Chen, H. 2017. The CarbonTracker Data Assimilation Shell (CTDAS) v1. 0: implementation and global carbon balance 2001–2015. *Geoscientific Model Development,* 10**,** 2785-2800. https://doi.org/10.5194/gmd-10-2785-2017

WMO, G. 2022. The state of greenhouse gases in the atmosphere based on global observations through 2021. *WMO Greenhouse Gas Bulletin*. https://library.wmo.int/doc_num.php?explnum_id=11352

Supporting Information

Text S1. The WDCGG global analysis method

The WDCGG method consists of seven separate steps. The full documentation can be found in Tsutsumi et al. (2009).

Step 1: Station selection based on traceability to the WMO standard scale

In order to avoid the potential biases that can be introduced by using different concentration scales, WDCGG only uses data from stations that report results traceable to the most recent CO_2 scale from the GAW Central Calibration Laboratories (CCL) assigned for that parameter. The current scale is the WMO standard scale WMO-CO2-X2019.

Step 2: Integration of parallel data from the same station

The WDCGG method uses continuous (hourly averaged) observations as these better represent the average concentrations compared to the flask-air samples taking during daytime once per two weeks. For remote stations where both flask and continuous data exist, NOAA found offsets between continuous and flask based monthly averages of 0.16-0.35 ppm (Tans et al., 1990)~~(Tans et al., 1990)~~, in less remote areas this difference can be expected to be larger. For selected stations flask data are used for gap filling when continuous data is lacking.

Step 3: Selection of stations suitable for global analysis

All of station data are normalized against the South Pole and averaged for the whole observation period. The normalized and averaged data points are plotted against latitude, and a curve is fitted by using a nearest-neighbour local-quadratic regression. The stations with normalized data locate outside the 3 standard deviations of the latitudinal fitted curve are excluded from the selection. This selection procedure is repeated until all stations in the selection locating within the 3 standard deviations of the latitudinal fitted curve. This procedure results in 139 stations remaining, which have a reasonable latitudinal scatter range (~~Figure~~ Fig. 1).

Step 4: Abstraction of a station's average seasonal variation expressed by the Fourier harmonics

The average seasonal variation is obtained from the longest continuous segment of data by using three Fourier harmonics. Here is loop procedure where the following processes a-d are repeated until neither the long-term trend nor the average seasonal variation changes: a). de-trend original data, b). apply the harmonics to obtain seasonality, c). de-seasonality from original data to obtain long-term trend, d) smooth the long-term trend by using low-pass filter (a cut-off frequency of 0.48 cycle / year). After reaching this condition the average seasonal variation is determined and subtracted from the full data which leaves us with deseasonalized data that still can contain gaps.

Step 5: Interpolation of data gaps

The gaps of the deseasonalized data are filled by linear interpolation. Subsequently, the CO_2 time series without gaps is the sum of the interpolated trend and the average seasonality.

Step 6: Extrapolation for synchronization of data period

Extrapolate the long-term trend to the synchronization period and then add the average seasonal variation to obtain the synchronized data. This is an optional step that is excluded in this analysis.

Step 7: Calculation of the zonal and global mean mole fractions, trends, and growth rates.

Global and hemispheric means, trends and growth rates are calculated by area-weighted averaging the zonal means over each latitudinal band (30°). The growth rate is determined by taking the first derivative of the long-term trend.

Text S2. The CTE station network

290 stations are evaluated in the CTE inversion, the observations come from the ObsPack data product (Schuldt et al.~~Kenneth N.~~, 2022). The measurement methods at the stations include surface-based, shipboard-based, tower-based and aircraft-based. In this study, we only focus on data derived from the first three measurement types (i.e. aircraft-based measurements are excluded), and in total 230 out of 290 stations are selected (~~Figure~~ Fig. 1). For the stations that have both surface-based and tower-based measurements, we used the tower-based measurements for analysis. For the stations that have tower-based measurements, we selected the highest measurement.

Text S3. Calculation of atmospheric CO_2 mass

CTE simulates 3D CO_2 mole fraction with 25 levels in the vertical direction. The CO_2 mass at each level of the atmosphere can be calculated as a function of air mass and CO_2 concentration by weight.

$$m_{CO_2} = Cw_{CO_2} * m_{air} \tag{1}$$

where m_{CO_2} is the mass of the CO_2, kg. Cw_{CO_2} is the CO_2 concentration by weight, w %. m_{air} is the mass of the air, kg. CO_2 concentration by weight is obtained by the formula below:

$$Cw_{CO_2} = Cv_{CO_2} * \frac{M_{CO_2}}{M_{air}} \tag{2}$$

where Cv_{CO_2} is the mole fraction of CO_2 in air, mol / mol. According to the ideal gas assumption, equal volume of gases at same temperature and pressure contains equal number of moles regardless of chemical nature of gases, i.e. the CO_2 concentration by mole equals the CO_2 concentration by volume. M_{CO_2} is the CO_2 molar mass (44.009 g/mol). M_{air} is the average molar mass of dry air (28.9647 g / mol).

Pressure is the force applied perpendicular to the surface of an object, therefore, air pressure can be expressed by:

$$p_{air} = \frac{F_{air}}{S} \tag{3}$$

where p_{air} is the pressure of air, Pa or N / m^2. In this case, p_{air} is the difference of air pressure between adjacent level boundaries, e.g. air pressure at level 1 is $p_1 - p_2$. F_{air} is the magnitude of the normal force of air or gravity of air, N or kg m / s^2. The gravity of air at each level can be estimated by:

$$F_{air} = m_{air} * g \tag{4}$$

where g is the gravitational field strength, about 9.81 m / s^2 or N / kg.

S is the area of the surface, m^2. Here S is the area of grid cell at each level, increasing with geopotential height (gph). It is calculated as a function of latitude and longitude on earth's surface, radius of the earth (R), and gph.

$$S = 2 * \pi * (R + gph)^2 * |\sin(lat1) - \sin(lat2)| * \frac{|lon1 - lon2|}{360} \tag{5}$$

Where, $lat1$, $lat2$, $lon1$and $lon2$ are the boundary of grid cell. R = 6378.1370 km, here we use the equatorial radius which is the distance from earth's center to the equator.

Hence the mass of the air in Eq. 1 can be estimated by:

$$m_{air} = \frac{p_{air} * S}{g} \tag{6}$$

Text S4. File list

All code necessary to calculate the global mean surface CO_2 mole fraction and Atmospheric CO_2 mass is freely available on ICOS Carbon Portal as a zipped archive (GAW_code.zip) [https://doi.org/10.18160/Q788-9081], when unzipped, the code include:

- fit_filter_~~seminoaa~~gfit.ipynb

  Apply the ~~semi-NOAA~~GFIT method to GAW observations (139 stations), CTE observations (230 stations), CTE model output at stations (230 stations) and CTE model output (full global)
- cal_zonal_global_co2_gaw_~~seminoaa~~gfit.ipynb

  Calculate global co2 mole fraction average and its growth rate, and estimate their uncertainty, using output from GAW(~~semi-NOAA~~GFIT)
- cal_zonal_global_co2_gaw_wdcgg.ipynb

  Calculate global co2 mole fraction average and its growth rate, and estimate their uncertainty, using output from GAW(WDCGG)
- cal_zonal_global_co2_ctracker_obs.ipynb

  Calculate global co2 mole fraction average and its growth rate, and estimate their uncertainty, using output from CTE_obs(~~semi-NOAA~~GFIT)
- cal_zonal_global_co2_ctracker_model_sample.ipynb

  Calculate global co2 mole fraction average and its growth rate, and estimate their uncertainty, using output from CTE_output(~~semi-NOAA~~GFIT)
- cal_zonal_global_co2_ctracker_model_global.ipynb

  Calculate global co2 mole fraction average and its growth rate, and estimate their uncertainty, using output from CTE_global(~~semi-NOAA~~GFIT)
- cal_co2mass_co2ppm_cte_global.ipynb

  Calculate global co2 mole fraction and global atmospheric co2 mass, using the 3D co2 output from CTE model
- compare_co2_co2rate.ipynb

  Statistically compare the co2 mole fraction and its growth rate among different data sources and analysis methods
- plot_results.ipynb

  The script is used to analyze and plot the results in the paper.

In order to run the jupyter ~~book~~notebooks, it needs to download the data (GAW_data.zip) [https://doi.org/10.18160/Q788-9081] and change the data path in jupyter notebooks to where the data is unzipped.

The key results with CSV format are accessible on ICOS Carbon Portal as a zipped archive (GAW_results.zip) [https://doi.org/10.18160/Q788-9081], when unzipped, the data include:

- Global monthly and annual surface CO_2 mole fraction and its growth rate for 1980-2020 derived from the GAW observations by using the ~~semi-NOAA~~GFIT method, i.e. GAW (~~semi-NOAA~~GFIT).

Global mean:

df_co2_annual_global_NH_SH_gaw_GFIT~~seminoaa~~.csv
df_co2_monthly_global_NH_SH_gaw_GFIT~~seminoaa~~.csv
df_co2rate_annual_global_NH_SH_gaw_GFIT~~seminoaa~~.csv
df_co2rate_monthly_global_NH_SH_gaw_GFIT~~seminoaa~~.csv

Their uncertainty basing on bootstrap method:

bootstats_co2_annual_global_gaw_GFIT~~seminoaa~~.csv
bootstats_co2_monthly_global_gaw_GFIT~~seminoaa~~.csv
bootstats_co2rate_annual_global_gaw_GFIT~~seminoaa~~.csv
bootstats_co2rate_monthly_global_gaw_GFIT~~seminoaa~~.csv

- Global monthly and annual surface CO_2 mole fraction and its growth rate for 1980-2020 derived from the GAW observations by using the WDCGG method without extrapolation, i.e. GAW (WDCGG).

Global mean:

df_co2_annual_global_NH_SH_gaw_wdcgg.csv
df_co2_monthly_global_NH_SH_gaw_wdcgg.csv
df_co2rate_annual_global_NH_SH_gaw_wdcgg.csv
df_co2rate_monthly_global_NH_SH_gaw_wdcgg.csv

Their uncertainty basing on bootstrap method:

bootstats_co2_annual_global_gaw_wdcgg.csv
bootstats_co2_monthly_global_gaw_wdcgg.csv
bootstats_co2rate_annual_global_gaw_wdcgg.csv
bootstats_co2rate_monthly_global_gaw_wdcgg.csv

- Global monthly and annual surface CO_2 mole fraction and its growth rate for 1980-2020 derived from the observations at the CTE 230 stations by using ~~semi-NOAA~~GFIT method, i.e. CTE_obs (~~semi-NOAA~~GFIT).

Global mean:

co2obs_co2_annual_global_NH_SH_ct2021_obs.csv
co2obs_co2_monthly_global_NH_SH_ct2021_obs.csv
co2obs_co2rate_annual_global_NH_SH_ct2021_obs.csv
co2obs_co2rate_monthly_global_NH_SH_ct2021_obs.csv

Their uncertainty basing on bootstrap method:

bootstats_co2_annual_global_cal_ct2021_obs.csv
bootstats_co2_monthly_global_cal_ct2021_obs.csv
bootstats_co2rate_annual_global_cal_ct2021_obs.csv
bootstats_co2rate_monthly_global_cal_ct2021_obs.csv

- Global monthly and annual surface CO_2 mole fraction and its growth rate for 2001-2020 derived from the CTE model output sampling at the CTE 230 stations by using ~~semi-NOAA~~GFIT method, i.e. CTE_output (~~semi-NOAA~~GFIT).

Global mean:

co2model_co2_annual_global_NH_SH_ct2021_modelsample.csv
co2model_co2_monthly_global_NH_SH_ct2021_modelsample.csv
co2model_co2rate_annual_global_NH_SH_ct2021_modelsample.csv
co2model_co2rate_monthly_global_NH_SH_ct2021_modelsample.csv

Their uncertainty basing on bootstrap method:

bootstats_co2_annual_global_cal_ct2021_modelsample.csv
bootstats_co2_monthly_global_cal_ct2021_modelsample.csv
bootstats_co2rate_annual_global_cal_ct2021_modelsample.csv
bootstats_co2rate_monthly_global_cal_ct2021_modelsample.csv

- Global monthly and annual surface CO_2 mole fraction and its growth rate for 2001-2020 derived from the CTE model output covers full global (averaged over the first three levels, 0 to 0.35 km Alt.) by using ~~semi-NOAA~~GFIT method, i.e. CTE_global (~~semi-NOAA~~GFIT)

co2_annual_global_cte2021(level1-3)_GFIT~~seminoaa~~.csv
co2_monthly_global_cte2021(level1-3)_GFIT~~seminoaa~~.csv
co2rate_annual_global_cte2021(level1-3)_GFIT~~seminoaa~~.csv
co2rate_monthly_global_cte2021(level1-3)_GFIT~~seminoaa~~.csv

- Global monthly and annual surface CO_2 mole fraction for 2001-2020 derived from the CTE model output covers full global with different heights (i.e. level1-3 and level1-25).

cte2021(lv1-3)_co2_2000_2020_annual.csv

cte2021(lv1-3)_co2_2000_2020_monthly.csv
cte2021(lv1-25)_co2_2000_2020_annual.csv
cte2021(lv1-25)_co2_2000_2020_monthly.csv

- Global monthly and annual atmospheric CO_2 mass (up to ~200 km) for 2000-2020 derived from the CTE model output by using the method described in Text S3.
  cte2021_co2mass_2000_2020_monthly.csv
  cte2021_co2mass_2000_2020_annual.csv

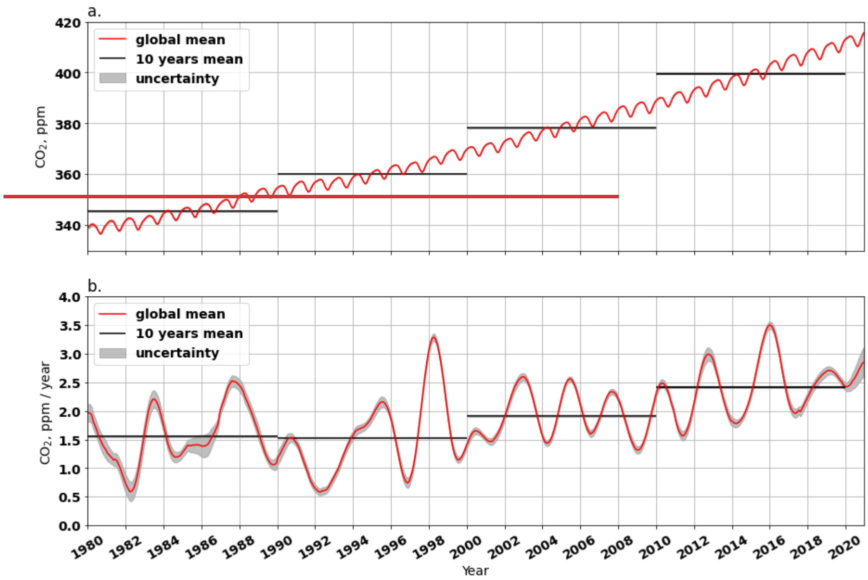
a.
420
400
380
360
340
global mean
10 years mean
uncertainty
CO2, ppm
b.
4.0
3.5
3.0
2.5
2.0
1.5
1.0
0.5
0.0
global mean
10 years mean
uncertainty
CO2, ppm / year
1980 1982 1984 1986 1988 1990 1992 1994 1996 1998 2000 2002 2004 2006 2008 2010 2012 2014 2016 2018 2020
Year

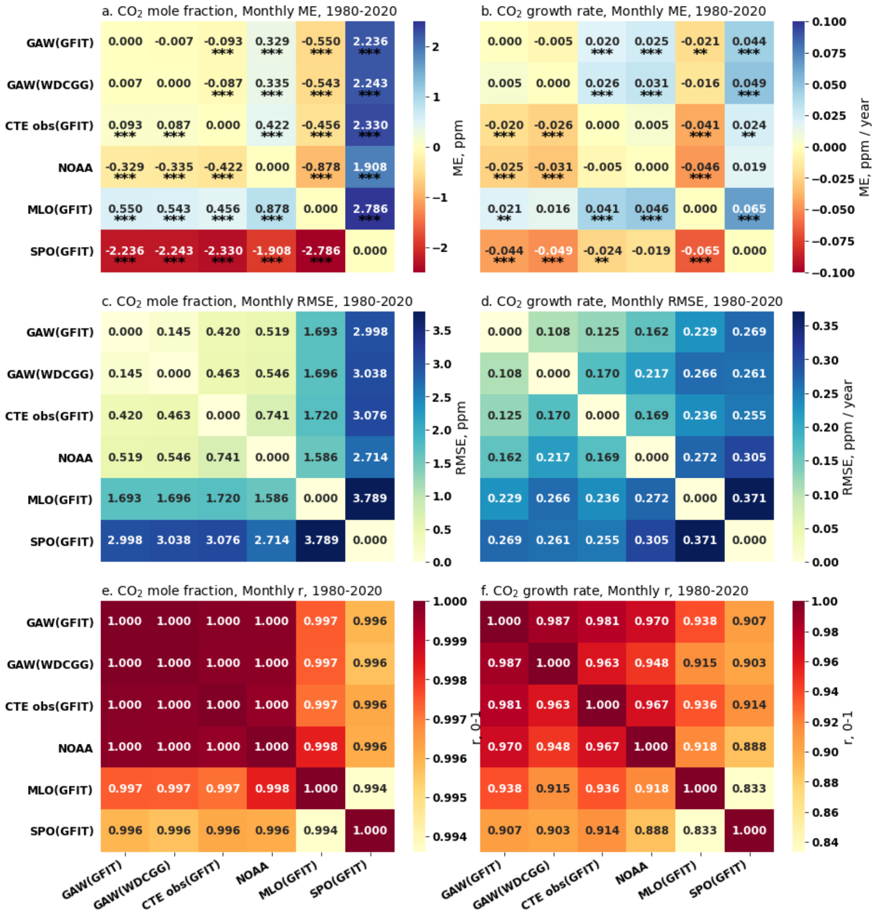

Figure S1. Pair-wise statistical metrics assess the agreement of monthly global and local CO_2 mole fraction (ppm) and its G_{ATM} (ppm yr-1) across various networks and methodologies (see Table 1 and Fig. 4) for the period 1980-2020. Panel (a) presents the Mean Error (ME) quantifying the difference for each pair, focusing on CO_2 mole fraction, while panel (b) does the same for G_{ATM}. The significance levels of paired t-test for ME are indicated as follows: * p<0.1, ** p<0.05, *** p<0.01. Panel (c) and (d) present the Root Mean Squared Error (RMSE) for CO_2 mole fraction and G_{ATM}, respectively. Panel (e) and (f) present the Pearson Correlation Coefficient (r) for CO_2 mole fraction and G_{ATM}, respectively.

Formatted: Subscript

Formatted: Subscript

~~Figure S1. Globally averaged CO_2 mole fraction (a) and its G_{ATM} (b) from 1980 to 2021. In panel (a), the red line shows the mean CO_2 mole fraction, black lines show the mean CO_2 mole fraction over 10 years, the grey area shows the uncertainty derived from the 200 bootstrap networks. Similarly, panel (b) shows the G_{ATM} instead of the mole fraction. The CO_2 and its G_{ATM} results are derived from the GAW observations from 139 stations by using semi-NOAA method.~~

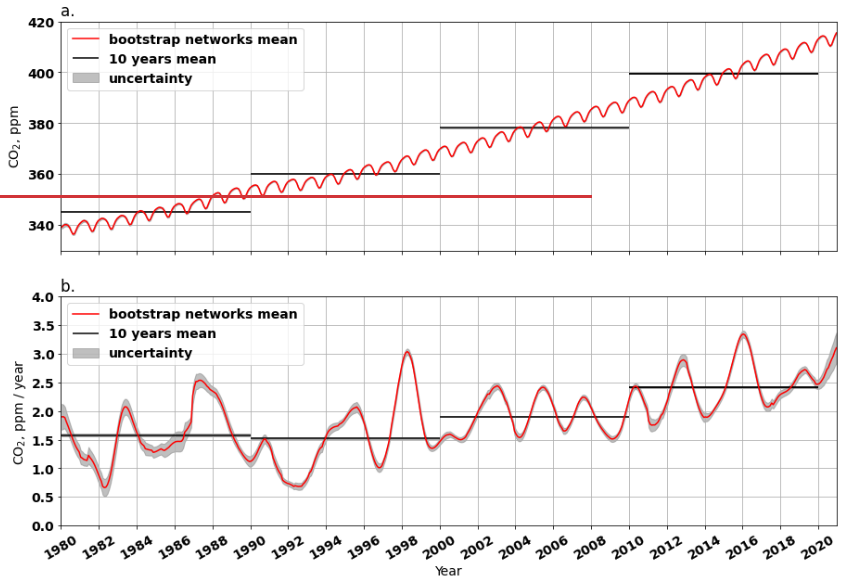
a.
bootstrap networks mean
10 years mean
uncertainty
CO$_2$, ppm
b.
bootstrap networks mean
10 years mean
uncertainty
CO$_2$, ppm / year
Year

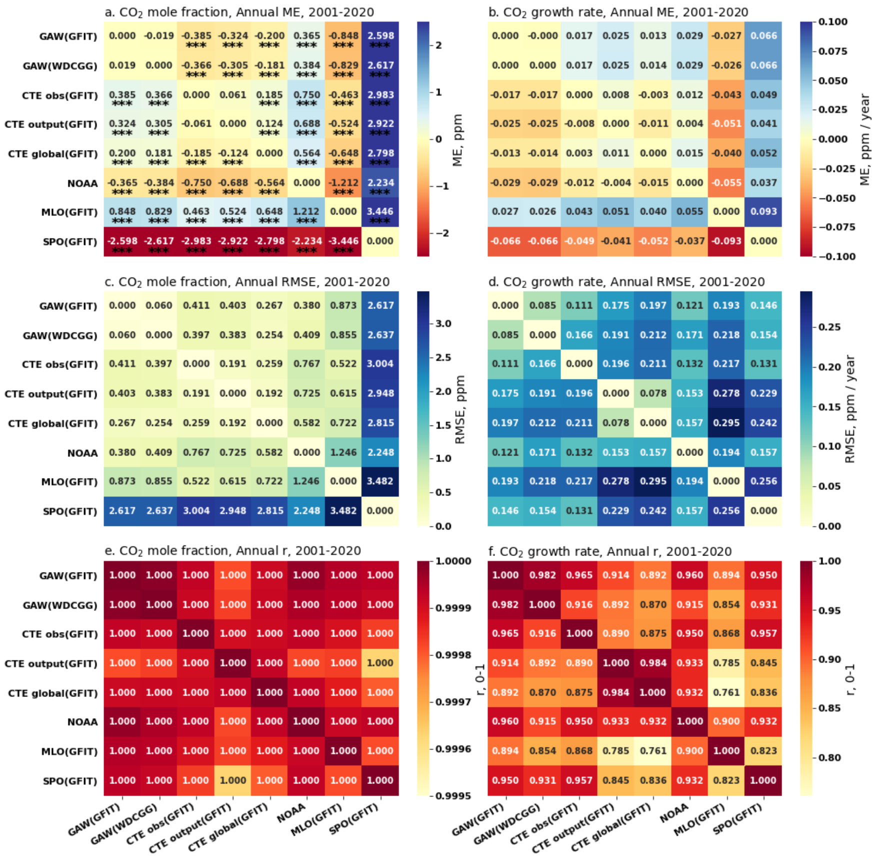

Figure S2. Pair-wise statistical metrics assess the agreement of annual global and local CO_2 mole fraction (ppm) and its G_{ATM} (ppm yr-1) across various networks and methodologies (see Table 1 and Fig. 4) for the period 2001-2020. Panel (a) presents the Mean Error (ME) quantifying the difference for each pair, focusing on CO_2 mole fraction, while panel (b) does the same for G_{ATM}. The significance levels of paired t-test for ME are indicated as follows: * p<0.1, ** p<0.05, *** p<0.01. Panel (c) and (d) present the Root Mean Squared Error (RMSE) for CO_2 mole fraction and G_{ATM}, respectively. Panel (e) and (f) present the Pearson Correlation Coefficient (r) for CO_2 mole fraction and G_{ATM}, respectively.

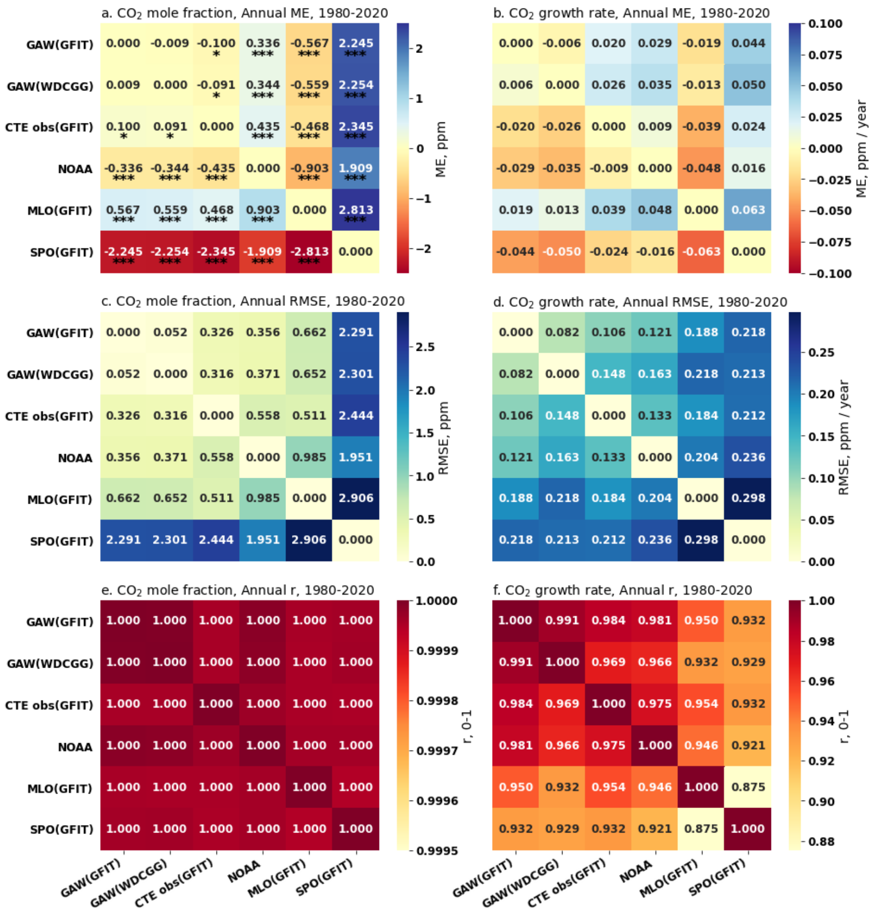

Figure S3. Pair-wise statistical metrics assess the agreement of annual global and local CO_2 mole fraction (ppm) and its G_{ATM} (ppm yr-1) across various networks and methodologies (see Table 1 and Fig. 4) for the period 1980-2020. Panel (a) presents the Mean Error (ME) quantifying the difference for each pair, focusing on CO_2 mole fraction, while panel (b) does the same for G_{ATM}. The significance levels of paired t-test for ME are indicated as follows: * p<0.1, ** p<0.05, *** p<0.01. Panel (c) and (d) present the Root Mean Squared Error (RMSE) for CO_2 mole fraction and G_{ATM}, respectively. Panel (e) and (f) present the Pearson Correlation Coefficient (r) for CO_2 mole fraction and G_{ATM}, respectively.

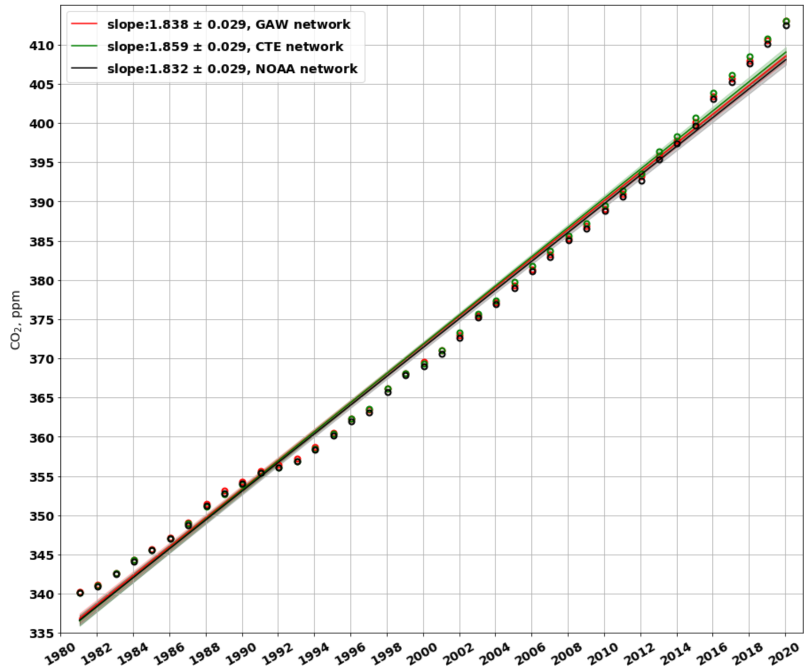

Figure S4. shows the trends of global CO_2 mole fraction for the GAW network (red line), the CTE network (green line) and the NOAA network (black line) during the whole period 1980-2020. The cycles show the annual CO_2 mole fraction, respectively.

Formatted: Font: Bold, Not Italic

Formatted: Font: Bold, Not Italic

Formatted: Font: Bold, Not Italic, Font color: Auto

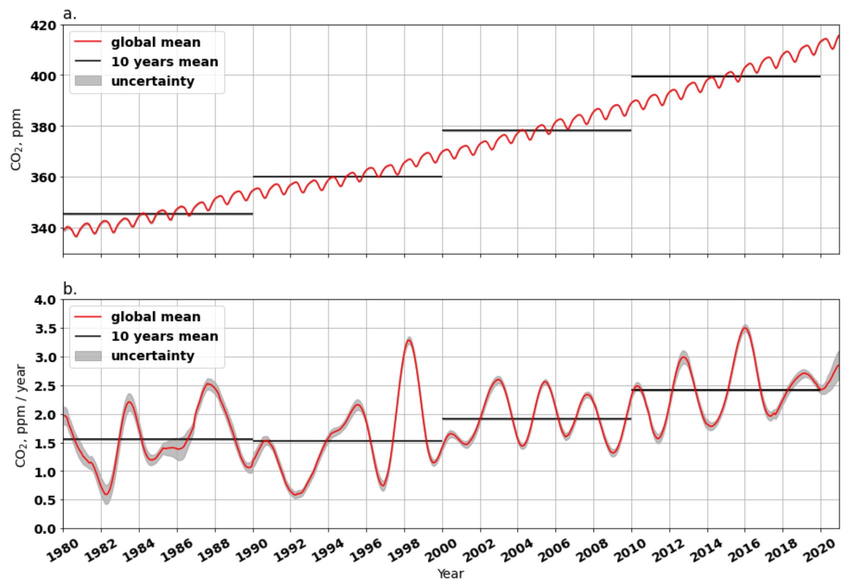

Figure S~~1~~5. Globally averaged CO_2 mole fraction (a) and its G_{ATM} (b) from 1980 to 202~~1~~0. In panel (a), the red line shows the mean CO_2 mole fraction, black lines show the mean CO_2 mole fraction over 10 years, the grey area shows the uncertainty derived from the 200 bootstrap networks. Similarly, panel (b) shows the G_{ATM} instead of the mole fraction. The CO_2 and its G_{ATM} results are derived from the GAW observations from 139 stations by using ~~semi-NOAA~~GFIT method.

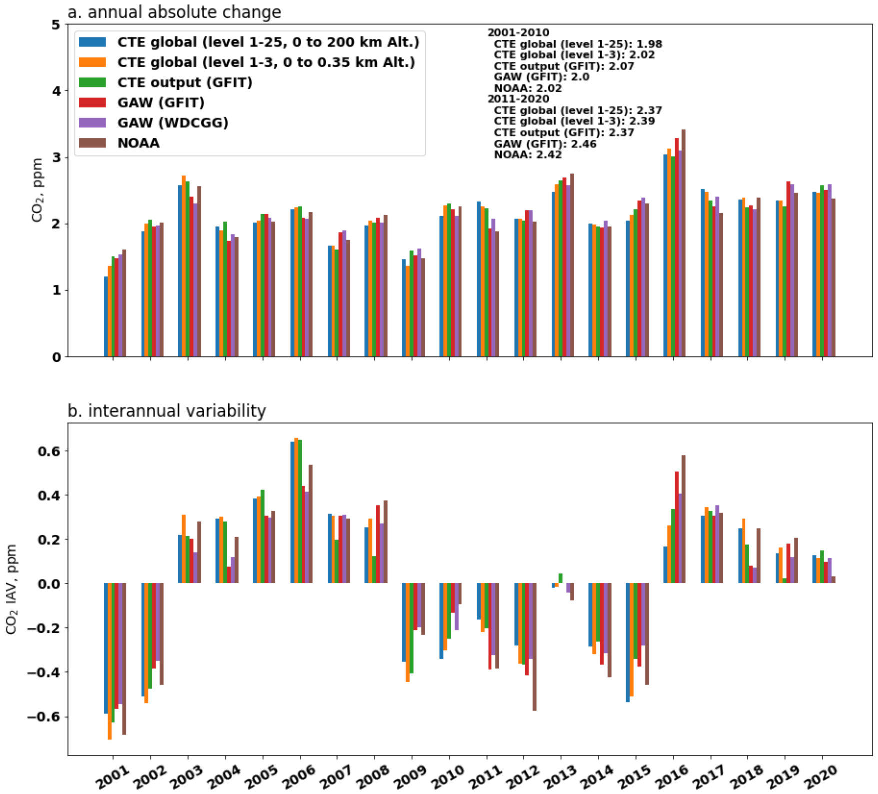

Figure 8S6. Annual absolute change and interannual variability of global CO_2 mole fraction derived from different data (CTE model, GAW observation and NOAA observation) and analysis methods (GFIT method, WDCGG method and NOAA method) for 2000-2020. Panel (a) shows the annual absolute change which is the difference between annal mean. Averages over 2001-2010 and 2011-2020 are also shown. Panel (b) shows the IAV which is calculated as the anomaly departure from a quadratic trend.

~~Figure S2. Globally averaged CO_2 mole fraction (a) and its G_{ATM} (b) from 1980 to 2021. In panel (a), black lines show the mean CO_2 mole fraction over 10 years, the grey lines show the 200 bootstrap networks, the red line shows the mean of the 200 bootstrap networks. Similarly, panel (b) shows the G_{ATM} results instead of CO_2 mole fraction. This result is derived from the GAW observations from 139 stations by using WDCGG method.~~

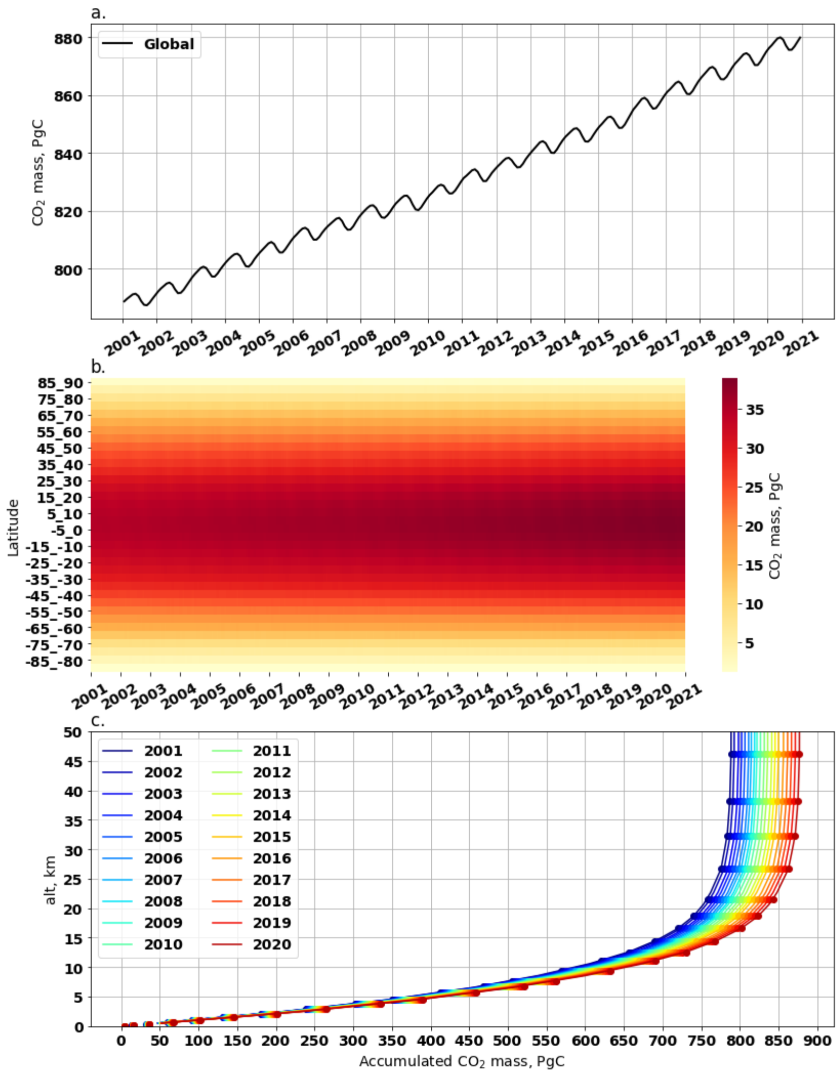

Figure ~~S3~~S7. Atmospheric CO_2 mass derived from CTE output. Panel (a) shows the global monthly CO_2 mass in atmosphere (from surface up to 200 km altitude). Panel (b) shows the zonal (5°) average of monthly CO_2 mass. Panel (c) shows accumulated CO_2 mass with altitudes from 2001 to 2020, the dots mark CTE vertical level altitudes and lines are the linear interpolation between the altitudes.

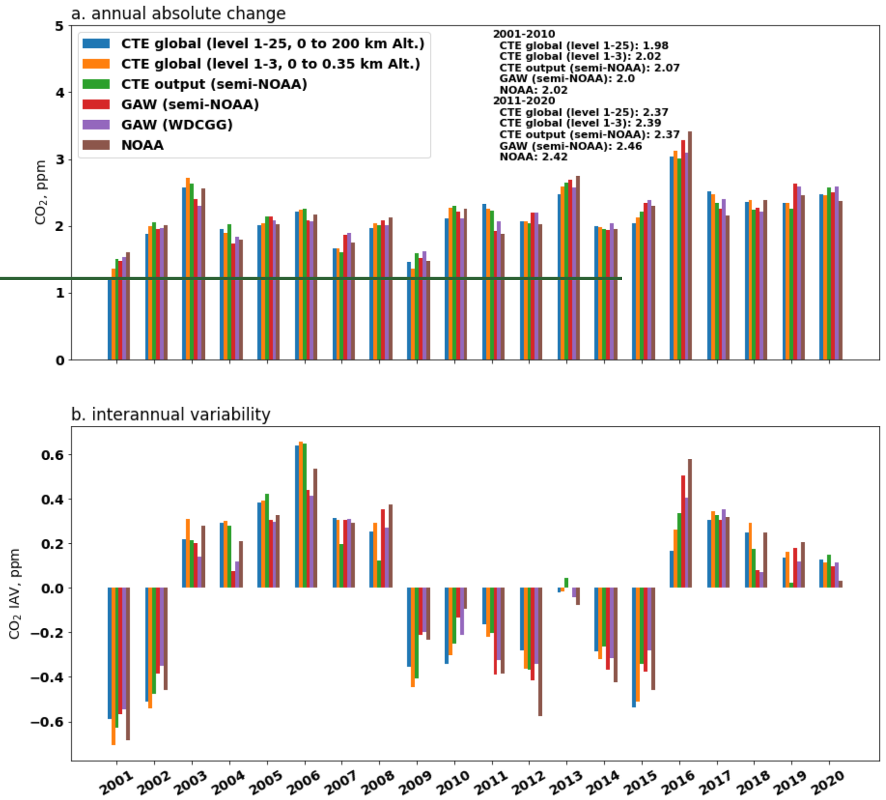

~~**Figure 8. Annual absolute change and interannual variability of global CO_2 mole fraction derived from different data (CTE model, GAW observation and NOAA observation) and analysis methods (semi-NOAA method, WDCGG method and NOAA method) for 2000-2020. Panel (a) shows the annual absolute change which is the difference between annal mean. Averages over 2001-2010 and 2011-2020 are also shown. Panel (b) shows the IAV which is calculated as the anomaly departure from a quadratic trend.**~~

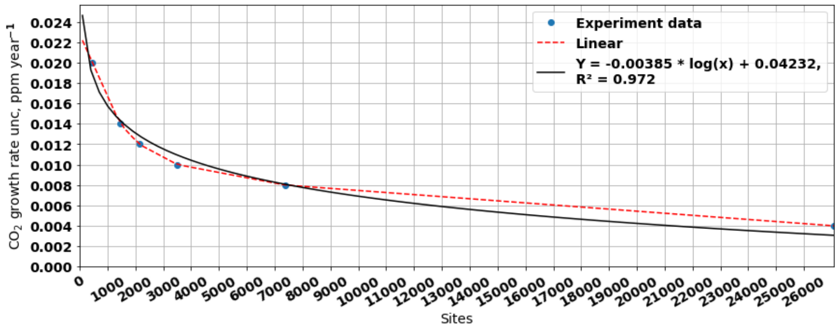

Figure ~~S4~~S8. The relationship between the uncertainty of the global CO_2 growth rate and the number of observation sites. The relationship is estimated using CTE_global (all global grids excluding ocean grids) with different resolutions (1x1, 2x2, 3x3, 4x4, 5x5, and 10x10 degrees) to estimate the uncertainty of the global CO_2 growth rate. The bootstrap method mentioned in the main text is used to estimate the uncertainty, and the results are represented as blue dots. The

red dashed line shows the linear interpolation between the experimental results, while the black line shows an exponential curve fitting.

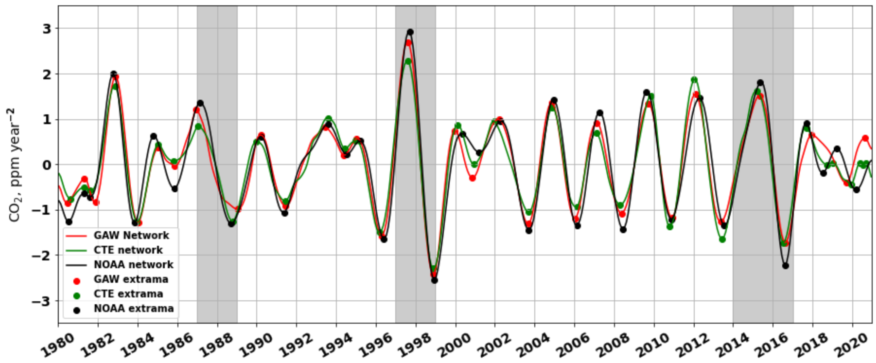

Figure S9, presents the smoothed trend of CO_2 growth rate for each month during 1980-2020. The trends (depicted in Figure 6b) are smoothed by using a Gaussian filter (with sigma=1.96). The dots represent the local extrema, which aid in identifying the start of CO_2 growth rate increase/decrease.

	~~a. GAW (WDCGG), 1980-2020~~				~~b. NOAA, 1980-2020~~			
	~~Annual~~		~~Monthly~~		~~Annual~~		~~Monthly~~	
~~Statistic~~	~~CO_2~~	~~G_{ATM}~~	~~CO_2~~	~~G_{ATM}~~	~~CO_2~~	~~G_{ATM}~~	~~CO_2~~	~~G_{ATM}~~
~~r~~	~~0.999~~	~~0.991~~	~~0.999~~	~~0.987~~	~~0.999~~	~~0.980~~	~~0.999~~	~~0.970~~
~~RMSE~~	~~0.053~~	~~0.081~~	~~0.145~~	~~0.108~~	~~0.352~~	~~0.121~~	~~0.519~~	~~0.162~~
~~MAE~~	~~0.043~~	~~0.070~~	~~0.114~~	~~0.086~~	~~0.329~~	~~0.094~~	~~0.449~~	~~0.129~~
~~ME~~	~~0.007~~	~~0.005~~	~~0.007~~	~~0.005~~	~~-0.329***~~	~~-0.025~~	~~-0.329***~~	~~-0.025***~~
	~~c. CTE_obs (semi-NOAA), 1980-2020~~				~~d. CTE_obs (semi-NOAA), 2001-2020~~			
~~r~~	~~0.999~~	~~0.984~~	~~0.999~~	~~0.981~~	~~0.999~~	~~0.963~~	~~0.999~~	~~0.961~~
~~RMSE~~	~~0.324~~	~~0.104~~	~~0.420~~	~~0.125~~	~~0.401~~	~~0.115~~	~~0.487~~	~~0.136~~
~~MAE~~	~~0.275~~	~~0.081~~	~~0.340~~	~~0.100~~	~~0.370~~	~~0.086~~	~~0.398~~	~~0.107~~
~~ME~~	~~0.093*~~	~~-0.020~~	~~0.093***~~	~~-0.020***~~	~~0.368***~~	~~-0.007~~	~~0.368***~~	~~-0.007~~
	~~e. CTE_output (semi-NOAA), 2001-2020~~				~~f. CTE_global (semi-NOAA), 2001-2020~~			
~~r~~	~~0.999~~	~~0.917~~	~~0.999~~	~~0.904~~	~~0.999~~	~~0.903~~	~~0.999~~	~~0.896~~
~~RMSE~~	~~0.395~~	~~0.174~~	~~0.476~~	~~0.214~~	~~0.261~~	~~0.192~~	~~0.347~~	~~0.230~~
~~MAE~~	~~0.348~~	~~0.131~~	~~0.389~~	~~0.174~~	~~0.220~~	~~0.158~~	~~0.279~~	~~0.195~~

Formatted: Keep with next

Formatted: Font: 10 pt

Formatted: Font: 10 pt

Formatted: Font: Bold, Subscript

Formatted: Font: 10 pt

Formatted: Font: Bold, Subscript

Formatted: Font: 10 pt

Formatted: Line spacing: 1.5 lines

Formatted: Centered

Formatted: Centered

Formatted: Centered

Formatted: Centered

Formatted: Centered

Formatted: Centered

Formatted: Centered

Formatted: Centered

Formatted: Centered

Formatted: Centered

Formatted: Centered

Formatted: Centered

Formatted: Centered

Formatted: Centered

Formatted: Centered

~~**ME**~~	~~0.299***~~	~~-0.015~~	~~0.299***~~	~~-0.015~~	~~0.186***~~	~~-0.012~~	~~0.186***~~	~~-0.012~~

~~Note paired t-test significant level for ME: * p<0.1, ** p<0.05, *** p<0.01~~

~~**Table S1. Statistic metrics assessing the agreement of the global CO_2 mole fraction (ppm) and its G_{ATM} (ppm yr^{-1}) from GAW observations (139 sties) using the semi-NOAA method (GAW (semi-NOAA)) with, a. GAW (WDCGG), GAW observations using the WDCGG method without extrapolation (1980-2020), b. NOAA analysis for observations from the NOAA 43 sites (1980-2020), c. CTE_obs (semi-NOAA), CTE observations (230 sites) using the semi-NOAA method (1980-2020), d. CTE observations (230 sites) using the semi-NOAA method (2001-2020), e. CTE_output(semi-NOAA), CTE output at the 230 sites using the semi-NOAA method (2001-2020), f. CTE_global (semi-NOAA), CTE full global grids (averaged over the first three levels, 0 to 0.35 km Alt.) using the semi-NOAA method (2001-2020). The statistical metrics include: Pearson Correlation Coefficient (r), which ranges from -1 to 1, Root Mean Squared Error (RMSE), Mean Absolute Error (MAE), and Mean Error (ME). The negative sign on ME means that the GAW (semi-NOAA) has higher values, vice versa.**~~

GAW (WDCGG+) vs GAW (WDCGG), 1984-2020				
	Annual		Monthly	
Statistic	CO_2	G_{ATM}	CO_2	G_{ATM}
r	0.999	0.994	0.999	0.992
RMSE	0.130	0.062	0.180	0.076
MAE	0.115	0.037	0.151	0.042
ME	0.096***	-0.011	0.096***	-0.011***

Note paired t-test significance~~t~~ level for ME: * p<0.1, ** p<0.05, *** p<0.01

Table ~~S2~~S1. Statistic metrics assessing the agreement of the global CO_2 mole fraction (CO_2, ppm) and its G_{ATM} (ppm yr^{-1}) from GAW (WDCGG) and GAW (WDCGG+) during common period 1984-2020. GAW (WDCGG) is GAW observations (139 sites) analysed by using the WDCGG method without extrapolation. GAW (WDCGG+) is GAW observations (139 sites) analysed by using the WDCGG method with extrapolation. The statistical metrics include: Pearson Correlation Coefficient (r), which ranges from -1 to 1, Root Mean Squared Error (RMSE), Mean Absolute Error (MAE), and Mean Error (ME). The negative values in ME means the GAW (WDCGG) has higher values, vice versa.

~~**CTE output (semi-NOAA) vs CTE obs (semi-NOAA), 2001-2020**~~				
	~~Annual~~		~~Monthly~~	
~~**Statistic**~~	~~CO_2~~	~~G_{ATM}~~	~~CO_2~~	~~G_{ATM}~~
~~**r**~~	~~0.999~~	~~0.896~~	~~0.999~~	~~0.881~~
~~**RMSE**~~	~~0.192~~	~~0.191~~	~~0.270~~	~~0.235~~
~~**MAE**~~	~~0.153~~	~~0.143~~	~~0.212~~	~~0.195~~
~~**ME**~~	~~-0.069~~	~~-0.008~~	~~-0.069***~~	~~-0.008~~

~~Note paired t-test significant level for ME: * p<0.1, ** p<0.05, *** p<0.01~~

~~**Table S3. Statistic metrics assessing the agreement of the global CO_2 mole fraction (CO_2, ppm) and its G_{ATM} (ppm yr^{-1}) from CTE_output (semi-NOAA) and CTE_obs (semi-NOAA) during common period 2001-2020. CTE_obs (semi-NOAA) is CTE observations (230 sites) analysed by using the semi-NOAA method. CTE_output (semi-NOAA) is CTE output at the 230 sites analysed by using the semi-NOAA method. The statistical metrics include: Pearson Correlation Coefficient (r), which ranges from -1 to 1, Root Mean Squared Error (RMSE), Mean Absolute Error (MAE), and Mean Error (ME). The negative values in ME means the CTE_obs (semi-NOAA) has higher values, vice versa.**~~

El Niño 1987-1988				
	Trough (G_{ATM} starts increasing)		Peak (G_{ATM} starts decreasing)	
Date	Decimal year	Days of year	Decimal year	Days of year
CTE	1985.791635	289	1987.041665	15

Formatted: Centered
Formatted: Centered, Line spacing: single
Formatted: Line spacing: single
Formatted: Centered, Line spacing: single
Formatted: Line spacing: single
Formatted: Centered, Line spacing: single
Formatted: Centered, Line spacing: single
Formatted: Line spacing: single
Formatted: Centered, Line spacing: single
Formatted: Line spacing: single
Formatted: Centered, Line spacing: single
Formatted: Line spacing: single
Formatted: Centered, Line spacing: single
Formatted: Line spacing: single
Formatted: Centered, Line spacing: single
Formatted: Line spacing: single
Formatted: Centered, Line spacing: single
Formatted: Line spacing: single
Formatted: Centered, Line spacing: single
Formatted: Centered, Line spacing: single
Formatted: Line spacing: single
Formatted: Centered, Line spacing: single
Formatted: Line spacing: single
Formatted: Centered, Line spacing: single
Formatted: Line spacing: single
Formatted: Centered, Line spacing: single
Formatted: Line spacing: single

GAW	1985.874965	319	1986.958295	350
NOAA	1985.874965	319	1987.124995	46
El Niño 1997-1998				
CTE	1996.208325	76	1997.624975	228
GAW	1996.291655	106	1997.624975	228
NOAA	1996.374985	137	1997.708305	259
El Niño 2014-2016				
CTE	2013.458315	167	2015.208325	76
GAW	2013.374985	137	2015.374985	137
NOAA	2013.541645	198	2015.374985	137

Table S2. displays the estimates of CO_2 growth rate increase/decrease for the three strong El Niño events (i.e 1987-1988, 1997-1998 and 2014-2016). These estimates are calculated from the smoothed trend of CO_2 growth rate based on CTE, GAW and NOAA networks (Fig. S9).

Formatted: Font: 10 pt, Font color: Auto

Formatted: Caption, Keep with next

Formatted: Caption